



Three-dimensional mechanical models for the June 2000 earthquake sequence in the south Iceland seismic zone

Loïc Dubois^a, Kurt L. Feigl^{a,*}, Dimitri Komatitsch^{b,c}, Thóra Árnadóttir^d, Freysteinn Sigmundsson^d

^a Laboratoire de Dynamique Terrestre et Planétaire CNRS UMR 5562, Université Paul Sabatier, Observatoire Midi-Pyrénées, 14 avenue Édouard Belin, 31400 Toulouse, France

^b Université de Pau et des Pays de l'Adour, CNRS and INRIA Sud-Ouest Magique-3D, Laboratoire de Modélisation et d'Imagerie en Géosciences UMR 5212, Avenue de l'Université, 64013 Pau Cedex, France

^c Institut Universitaire de France, 103 boulevard Saint Michel, 75005 Paris, France

^d Nordic Volcanological Center, Institute of Earth Sciences, University of Iceland, Reykjavik, Iceland

ARTICLE INFO

Article history:

Received 11 September 2007

Received in revised form 3 May 2008

Accepted 12 May 2008

Available online 27 May 2008

Keywords:

South Iceland seismic zone

Lithospheric heterogeneity influences

Finite-element method

Co-seismic slip estimation

Coulomb stress changes

Seismicity migration

ABSTRACT

A sequence of earthquakes, including two $M_w=6.5$ events, occurred in June 2000 in an atypical transform zone located in the southwest of Iceland. The inter-, co-, and post-seismic time intervals of the associated deformation cycle have been well recorded by previous geodetic studies, including GPS and InSAR. Using a numerical code based on a finite-element method, we analyze the influence of structural and rheologic heterogeneities on the earthquake deformation cycle within the south Iceland seismic zone (SISZ). The co-seismic deformation is especially sensitive to the increase of lithospheric stiffness with depth, as shown by a joint inversion of the geodetic data. The estimated distribution of co-seismic slip for the June 21 mainshock is deeper when estimated in a realistic layered lithospheric model than in a homogenous half-space. The geometry of the rheologic layers also plays an important role during the post-seismic interval, when several inter-related processes (poro-elastic effects around the fault plane, afterslip in it, and/or visco-elastic relaxation in the lower crust and/or upper mantle) appear to occur on overlapping time and length scales. We also consider the seismicity, both in its contribution to stress transfer and in its tendency to migrate from east to west. At least six processes may be involved in changing the stress distribution: (1) propagation of seismic waves, (2) changes of static stress caused by major co-seismic slip, (3) cascading seismicity, (4) fluctuations in hydrological conditions, (5) ductile flow of subcrustal rocks, and (6) inter-seismic strain accumulation. All six of these phenomena occurred in the SISZ before, during and after the June 2000 earthquake sequence. By using three-dimensional finite-element models with realistic geometric and rheologic configurations to match the observations, we test the influence of the increase of rigidity with depth and the variable crustal thickness on processes (2), (3), (5) and (6). Inter-seismic strain (6) accumulating in an elastic upper crust that thickens eastward can produce an asymmetric stress distribution. This process may explain the tendency of subsequent earthquakes to migrate from east to west across the south Iceland seismic zone within a single sequence. Yet it cannot explain their timing or the location of the first event. Our modeling with realistic geometric and rheologic configurations suggests that the June 17 earthquake triggered the June 21 event by a combination of several time-dependent post-seismic processes.

© 2008 Elsevier B.V. All rights reserved.

1. Introduction

The south Iceland seismic zone (SISZ) is located on the boundary between the North America and Eurasia plates and it partly accommodates their relative motion as earthquakes. The plate boundary follows the spreading mid-Atlantic ridge, comes ashore on the Reykjanes peninsula (RP), where it becomes a shear zone to reach the western volcanic zone (WVZ) at a triple point near the Hengill

volcanic center (Fig. 1). There, most of the present-day deformation continues across the SISZ to the eastern volcanic zone. Overall, the SISZ accommodates left-lateral shear along its east-to-west trend, but most of the large ($M \sim 6$) earthquakes there rupture with right-lateral strike slip on vertical faults striking north. These parallel faults are 10–20 km long and ~5 km apart, analogous to books on a shelf (Einarsson et al., 1981). Indeed, the SISZ deforms as a shear zone, accommodating 18.9 ± 0.5 mm/yr of relative plate motion (DeMets et al., 1990, 1994) in a band less than 20 km wide (Sigmundsson et al., 1995). Consequently, the inter-seismic strain rate is $\sim 10^{-6}$ per year. The kinematics can be described as a locked fault zone slipping at a rate of 19 mm/yr below ~16 km depth (Árnadóttir et al., 2006). If accumulated elastically over a century, this strain could be released as ~2 m of co-seismic slip.

* Corresponding author. Department of Geology and Geophysics, University of Wisconsin–Madison, 1215 West Dayton Street, Madison, WI 53706, USA. Tel.: +1 608 262 8960; fax: +1 608 262 0693.

E-mail address: feigl@wisc.edu (K.L. Feigl).

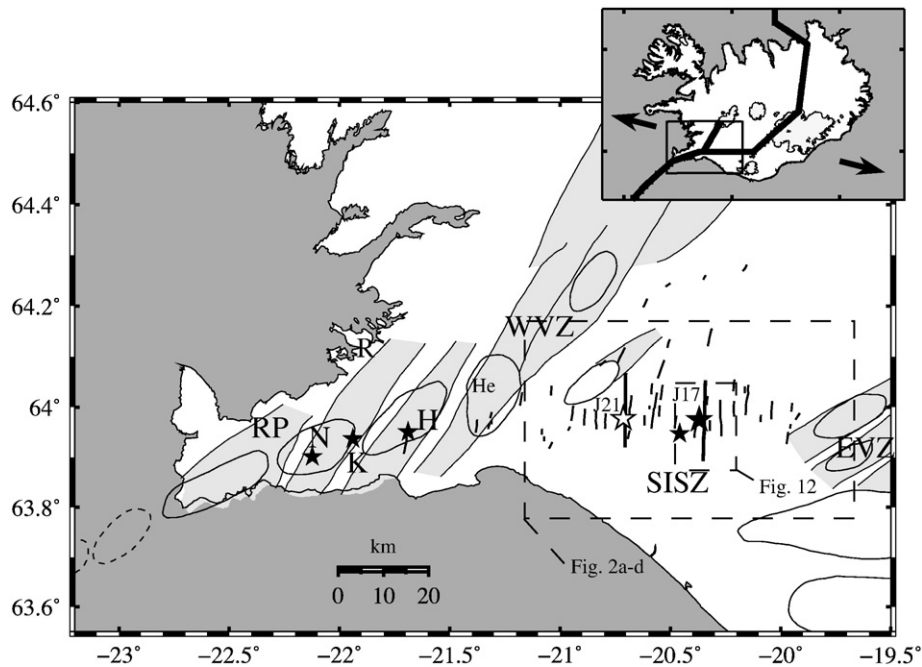


Fig. 1. Map showing the main tectonic features of the study area from Árnadóttir et al. (2004). The Reykjanes peninsula (RP), the Hengill triple junction (He), the western volcanic zone (WVZ), the south Iceland seismic zone (SISZ), and the eastern volcanic zone (EVZ) are indicated. The light shaded areas are individual fissure swarms with associated central volcanoes, which characterize the rift zones. Mapped surface faults of Holocene age are shown with black lines (Einarsson and Sæmundsson, 1987). The epicenter locations of earthquakes (mainshock and aftershocks) on June 17, 2000 are shown with black stars. The June 17 mainshock is labeled J17. The Reykjanes peninsula events occurred 26 s after J17 on the Hvalhnúkur fault (H), 30 s after J17 near Lake Kleifarvatn (K), and 5 min after J17 at Núpshlíðarháls (N) as located and timed by seismology (Vogfjörð, 2003; Antonioli et al., 2006). The location of the June 21, 2000 mainshock is shown with a white star labeled J21. The location of the capital of Iceland, Reykjavik, is denoted by R. Large and small dashed rectangles mark the areas shown in Figs. 2a–d and 12, respectively. The inset shows a simplified map of the plate boundary across Iceland, with the location of the main part of the figure indicated by the black rectangle. The black arrows show the relative motion between the North America and Eurasian plates from NUVEL-1A (DeMets et al., 1990, 1994).

Earthquakes in the SISZ do not rupture its entire 100-km length from east to west; the 20-km length of the north–south faults seems to limit their magnitude to 6.5 or 7.

The analyzed seismic sequence began on 17 June 2000, with a mainshock of magnitude $M_s=6.6$ (Antonioli et al., 2006). It produced co-seismic deformation that was measured geodetically by both GPS (Árnadóttir et al., 2001) and InSAR (Pedersen et al., 2001). Three and a half days (81 h) later, a second earthquake of the same magnitude ruptured a distinct fault some 18 km to the west of the first event. Both earthquakes have strike-slip focal mechanisms on faults dipping nearly vertically (Ekström et al., 2005) and ruptured the ground surface in a right-lateral, *en échelon* pattern with an overall strike within a few degrees of north (Clifton and Einarsson, 2005). The hypocentral depths estimated from seismology using a layered velocity model are 6.3 and 5.1 km for the June 17 and 21 mainshocks, respectively (Árnadóttir et al., 2001). The slip distributions estimated from geodetic data for both earthquakes have maxima over 2 m, down-dip widths of 10–12 km, and along-strike lengths of 16–18 km (Árnadóttir et al., 2001; Pedersen et al., 2003). The estimated geodetic magnitudes for the June 17 and June 21 slip distributions are $M_w=6.4$ and $M_w=6.5$, respectively (Pedersen et al., 2003).

The earthquakes in the 2000 SISZ sequence appear to be causally related. Just after the June 17 mainshock, additional earthquakes struck the Reykjanes peninsula, as far as 80 km to the west of the June 17 epicenter. Three of these events generated co-seismic displacements that were large enough to be measured by InSAR and GPS and to be modeled as dislocation sources (i.e. discontinuity in displacement in the fault plane) with magnitudes between $M_w=5.3$ and $M_w=5.8$ (Pagli et al., 2003). These secondary earthquakes ruptured the surface, broke rocks, and coincided with a drop of several meters in the water level of Lake Kleifar (Clifton et al., 2003). Three aftershocks, at 8 s, 26 s, and 30 s (Fig. 1) after the June 17 mainshock at 15:40:41 UTC seem to have been dynamically triggered by the seismic wave train as it propagated

westward (Antonioli et al., 2006). Two other events occurred 2 and 5 min after the June 17 mainshock at a distance of almost 4 km and 80 km towards the west, respectively (Antonioli et al., 2006). The June 17 earthquake brought the June 21 fault closer to failure, based on the increase in static Coulomb stress calculated at the June 21 hypocenter (Árnadóttir et al., 2003).

The migration of $M \geq 6$ earthquakes from east to west across the SISZ has been observed in previous earthquake sequences in 1732–1734, 1784, and 1896 (Einarsson et al., 1981; Scholz, 2002). In 1896, for example, five strong earthquakes ruptured distinct sub-parallel faults over a distance of 50 km during an interval of three weeks (Einarsson et al., 1981; Scholz, 2002). The $M \sim 7$ event in 1912, however, does not appear to fit this pattern because it occurred to the east of the 1896 sequence (Bjarnason et al., 1993a; Bellou et al., 2005).

In this study, our first objective is to evaluate the influence of geometric and rheologic lithospheric heterogeneities on the inter-, co-, and post-seismic deformation and stress fields in the SISZ. To explain the co-seismic deformation, we build on previous estimates of the distribution of slip that occurred on the rupture surfaces of the two mainshocks in June 2000 from GPS measurements of displacements (Árnadóttir et al., 2001), InSAR recordings of range change (the component of displacement along the line of sight from the ground to the satellite) analyzed by Pedersen et al. (2001), and a combination of both in a joint inversion (Pedersen et al., 2003). All three of these studies assume an elastic half-space with uniform values of shear modulus (or rigidity) μ and Poisson's ratio ν . Yet previous studies outside of Iceland suggest that assuming homogeneity can bias estimates of slip distribution (Cattin et al., 1999; Masterlark, 2003; Cianetti et al., 2005). For example, the aftershock hypocenters located by seismological methods are deeper than the bottom of the fault rupture inferred from geodetic measurements in the case of the 1994 Northridge earthquake in California (Hudnut et al., 1996). In other words, the seismological and geodetic procedures for locating co-seismic slip will

yield different estimates if they assume different elastic models. A similar discrepancy between the deepest aftershocks and the bottom of the slip distribution also appears to apply to the June 2000 sequence in the SISZ. Although the slip diminishes to less than 1 m below 8 km depth (Pedersen et al., 2003), the relocated aftershock hypocenters reach down to 10 km, with a few as deep as 12 km (Hjaltadóttir et al., 2005). Furthermore, the estimated slip distribution is sensitive to the material properties and fault geometry, especially the shear modulus (rigidity) μ in the upper crust (Dubois, 2006). By using layered models that account for increasing rigidity with depth, we expect deeper slip distributions (Cattin et al., 1999; Hearn and Burgmann, 2005). Furthermore, an accurate estimate of the slip distribution is required to test the hypothesis that *M* 6 earthquakes in the SISZ rupture into the lower crust (Stefánsson et al., 1993). Accurate estimates of slip distribution are also important for calculating maps of induced stress changes and assessing seismic hazard. Accordingly, we evaluate the effects of geometric and rheologic lithospheric heterogeneities in the inter- and post-seismic time intervals, especially in terms of stress changes. All of our stress calculations in a particular model are consistent with the slip distribution estimated with the same model. This strategy, suggested by Masterlark et al. (2001), avoids biasing the results.

Our second objective is to understand why seismicity appears to migrate from east to west across the SISZ. As on the North Anatolian fault in Turkey, it appears that one earthquake can trigger the next one (Barka, 1996; Stein et al., 1997; Hubert-Ferrari et al., 2000; Parsons et al., 2000). Unlike Turkey, where successive earthquakes rupture different segments of the same contiguous fault, the sequences in Iceland involve distinct parallel faults, separated by roughly one (~10 km) fault dimension. Although static Coulomb stress changes can explain the location of the triggered earthquakes, this simple theory cannot explain the time delay between the “source” (triggering) and “receiver” (triggered) events, as pointed out by Scholz (1990, 2002) and recently reviewed by Brodsky and Prejean (2005). At least six processes may be involved in transferring stress from one fault to another: (1) propagation of seismic waves, (2) changes in the static stress field caused by major co-seismic slip, (3) seismicity “cascading” in an aftershock sequence, (4) fluctuations in hydrological conditions, (5) flow of ductile rocks, and (6) inter-seismic strain accumulation. All six of these phenomena occurred in the SISZ before, during, and after the June 2000 events.

1. The dynamic stress changes caused by propagation of seismic waves apparently triggered the earthquakes on the Reykjanes peninsula in the first minute following the June 17 mainshock (Antonoli et al., 2006). Although this process is beyond the scope of our study, introducing the geometric and rheologic heterogeneities considered here into seismological models would presumably improve the accuracy of the synthetic seismograms (e.g., Komatitsch et al., 2004).
2. During an earthquake, the co-seismic slip on the fault plane permanently alters the stress field in the surrounding rock. By resolving the stress tensor onto a fault plane with a specified orientation, one can evaluate whether it is more or less likely to fail in a future earthquake based on the Coulomb failure stress changes. This calculation has been performed previously using a homogeneous half-space for the June 17 and 21 events in the SISZ (Árnadóttir et al., 2003), as well as for many other earthquake sequences, especially in strike-slip settings such as California (e.g., King et al., 1994; Stein, 1999).
3. In the “cascading seismicity” hypothesis, one earthquake triggers the next in a kind of seismic “domino effect”. Changes in static stress could alter rate- and state-dependent friction, thus producing a finite time delay between successive earthquakes (e.g., Toda et al., 2005). Here, we evaluate if the aftershock seismicity

in the June 2000 sequence changed the stress field enough to modify the assessment of seismic hazard (e.g., Helmstetter et al., 2005).

4. Fluctuations in hydrological conditions occurred in the weeks to months after the June 17 mainshock (Björnsson et al., 2001; Jónsson et al., 2003). Poro-elastic effects can explain about half the post-seismic signal in an interferogram spanning June 19 through July 24 in the SISZ (Jónsson et al., 2003). The same effects might also explain stress transfer in the 2000 SISZ sequence. Under this hypothesis, the co-seismic perturbation to the hydrologic pressure field also alters the stress conditions on faults near the mainshock, triggering aftershocks in areas where increasing pressure and shear stress respectively unclamps and leads faults near failure (Nur and Booker, 1972; Noir et al., 1997).
5. Viscous flow in ductile rocks occurs in the months to years after an earthquake. For example, post-seismic deformation has been recorded by GPS around the June 2000 faults as late as May 2004 (Árnadóttir et al., 2005). These centimeter-sized displacements have been modeled using a visco-elastic Burger’s rheology in a semi-analytical spherical-harmonic formulation by Árnadóttir et al. (2005). Here, we use a linear Maxwell visco-elastic rheology in a Cartesian finite-element formulation to investigate the effect of geometry and other rheologic parameters on stress changes due to viscous relaxation. Although ductile flow is much too slow to explain the 86-hour time delay between the June 17 and June 21 events, it may contribute to the time delays (~100 years) between earthquake sequences in the SISZ.
6. In terms of moment, the main events in the June 2000 sequence released only about a quarter of the strain accumulated since 1912, the date of the last major earthquake in the SISZ, assuming a constant strain rate over the intervening 88 years (Sigmundsson et al., 1995; Pedersen et al., 2003). Such inter-seismic strain accumulation could conceivably increase the stress in the SISZ and drive faults there closer to failure. Assuming that the crust thickens from west to east, we describe the elastic properties at a given depth as stiffer in the west than in the east. As a result, a uniform strain field that is imposed as far-field boundary conditions will lead to an asymmetric stress field that has higher stresses in the west than in the east. Furthermore, if the crust is considered as a thin plate, there will be an accumulation of stress in the thinnest (western) part. The resulting stress gradient could be steep enough to cause earthquakes to occur preferentially in the west.

All these considerations motivate us to move beyond the approximation of a half-space with uniform elastic properties used in previous co-seismic studies and beyond the horizontal layering approximation used in the visco-elastic models. In this study, we explore models with rheologic and geometric heterogeneities, such as dipping layers with variable thickness and/or a weak fault damage zone around the mainshock faults. To do so, we calculate stress and displacement fields using a finite-element method (e.g., Dhatt and Touzot, 1984). We use the TECTON code, renovated by Williams and Richardson (1991), as described below. This approach allows us to account for the variations in material properties (density, shear modulus, and Poisson’s ratio) and their geometric configuration inferred from earthquake hypocenter locations (Stefánsson et al., 1993), seismic tomography (Bjarnason et al., 1993b; Darbyshire et al., 1998; Allen et al., 2002; Tryggvason et al., 2002), and gravity modeling (Menke, 1999; Darbyshire et al., 2000; Kaban et al., 2002).

2. Data

In this study, we consider different types of data: interferometric analysis of synthetic aperture radar images (InSAR), displacement

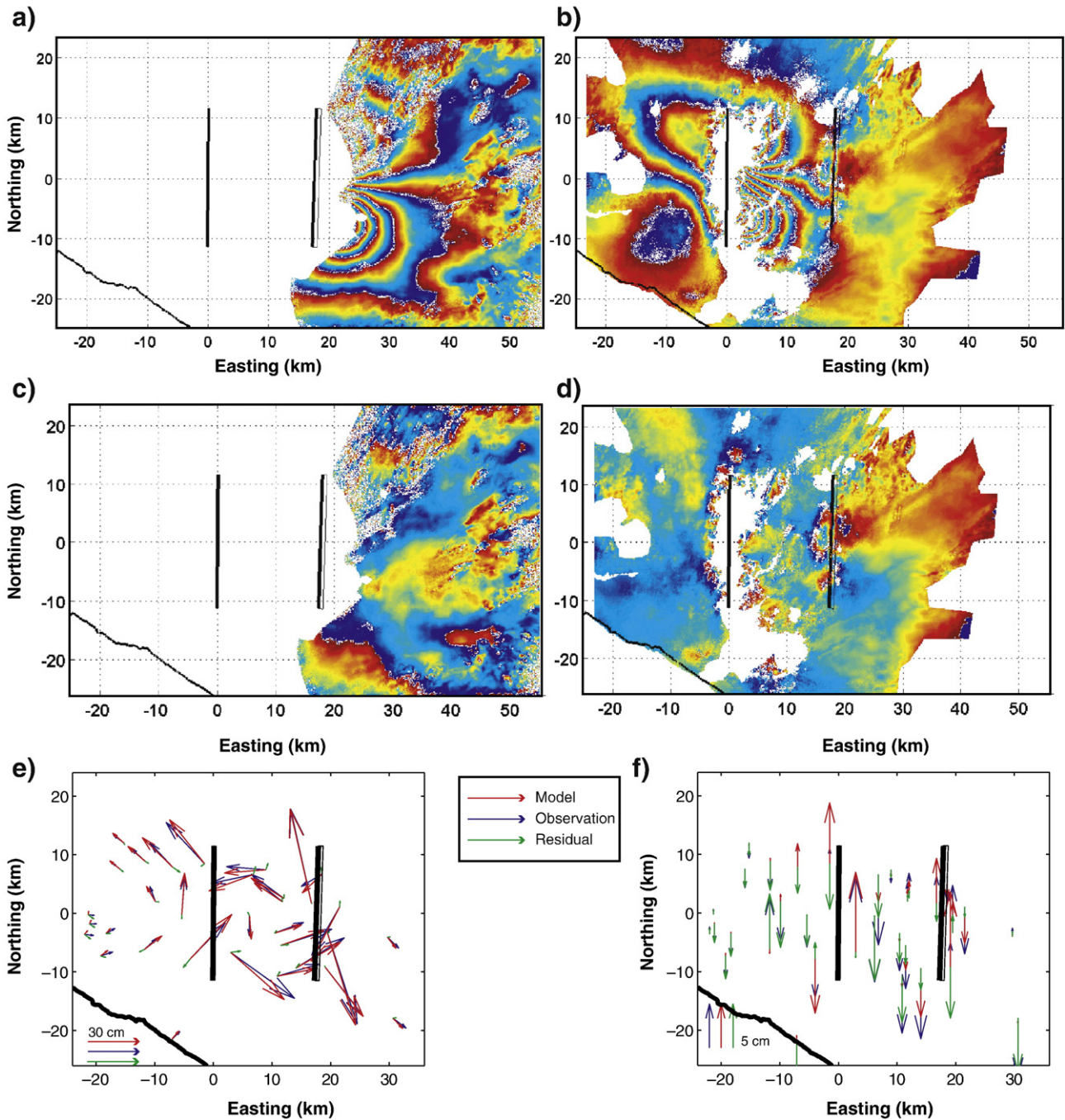


Fig. 2. Co-seismic interferograms (a–b) and GPS displacements (e–f), showing ground deformation created by the June 17 and June 21 earthquakes. One colored fringe corresponds to 28.4 mm of range change. The images have been corrected for orbital errors. Surface projections of the modeled dislocations related to the June 17 (east) and June 21, 2000 (west) earthquakes are drawn in black. The black line represents the Icelandic coast. (a) Interferogram T52 spans the time from June 16 to July 21, 2000. Therefore this interferogram includes deformation due to both $M_w=6.5$ mainshocks. (b) Interferogram T95 spans the time from June 19 to July 24, 2000. Therefore this interferogram includes the co-seismic deformations from the June 21 (west) mainshock and post-seismic deformation following the June 17 (east) mainshock. (c) Residual T52 interferogram showing the difference between the observed and modeled deformation fields using the “Iceland” configuration. Other configurations yield similar results (Dubois, 2006). (d) Residual T95 interferogram between observed and modeled deformation field using the “Iceland” configuration. Other configurations yield similar results (Dubois, 2006). Note the post-seismic signal near the June 17 (east) fault interpreted by Jónsson et al. (2003) as poro-elastic relaxation. (e) Comparison between the horizontal displacements measured by GPS (in blue) and those modeled using the “Iceland” configuration (in red). Other configurations yield similar results (Dubois, 2006). Residuals are represented in green. (f) Same as (e) but for the vertical components of the displacements.

vectors from GPS stations, location, focal mechanisms, and magnitude of the events in the June 2000 sequence.

The crustal deformation that occurred between June and September 2000 was recorded by the ERS-2 satellite in descending passes, with incidence angles varying from 19° to 27° . The acquired images have been described previously (Pedersen et al., 2001, 2003). The data set used here is the same as that analyzed by Pedersen et al. (2003). It

consists of two interferograms in ERS tracks T52 and T95. The T52 interferogram (Fig. 2a) covers an area just east of the June 17 fault and spans the time from June 16 to July 21, 2000. Interferogram T95 (Fig. 2b) covers a larger part of the SISZ. With a time span from June 19 to July 24, 2000, the T95 interferogram includes the June 21 event and some early post-seismic deformation near the June 17 fault. The latter signal has been interpreted as poro-elastic relaxation (Jónsson et al.,

2003). The useful part of these interferograms consists of 582 data points (179 for T52 and 403 for T95), which have been selected by Pedersen et al. (2003) using a two-dimensional quantization algorithm (Welstead, 1999).

The co-seismic GPS data set is the same as that used previously to estimate the distribution of slip on the faults that ruptured on June 17 and 21 (Árnadóttir et al., 2001; Pedersen et al., 2003). It includes displacement vectors from 37 stations. These stations have been surveyed in 1995, 1999, and 2000. The inter-seismic motion during the 5-year time interval has been subtracted to obtain the co-seismic GPS measurements. The stations are fairly evenly distributed in the area (Fig. 2e and f) and provide valuable information west of the June 17 fault.

The post-seismic GPS data set has been previously described by Árnadóttir et al. (2005). It includes 36 velocity vectors from 2000 to 2001 and 52 velocity vectors from 2001 to 2004, that have been corrected for the inter-seismic motion inferred from three surveys in 1992, 1995, and in 1999. In this study, we use the 2000–2001 veloci-

ties without subtracting the poro-elastic deformation calculated in Árnadóttir et al. (2005) using the homogeneous model of complete poro-elastic relaxation from Jónsson et al. (2003) (see the discussion in Section 6).

The earthquakes recorded by the SIL seismological network (Stefánsson et al., 1993; Bödvarsson et al., 1999) operated by the Icelandic Meteorological Office (IMO, 2006) have been relocated by Hjaltadóttir et al. (2005) using multiplet algorithms (Slunga et al., 1995; Slunga, 2003) to establish a data set of locations with a precision better than 1 km in all three spatial coordinates (Vogfjörd, 2003; Hjaltadóttir et al., 2005) as part of the PREPARED project (Stefánsson, 2006). We use this data set to account for the aftershocks.

3. Model

In order to account for vertical and horizontal gradients of the elastic parameters and fault damage zones (weaker zones centered on the faults) in the co-seismic inversion, we define five configurations of

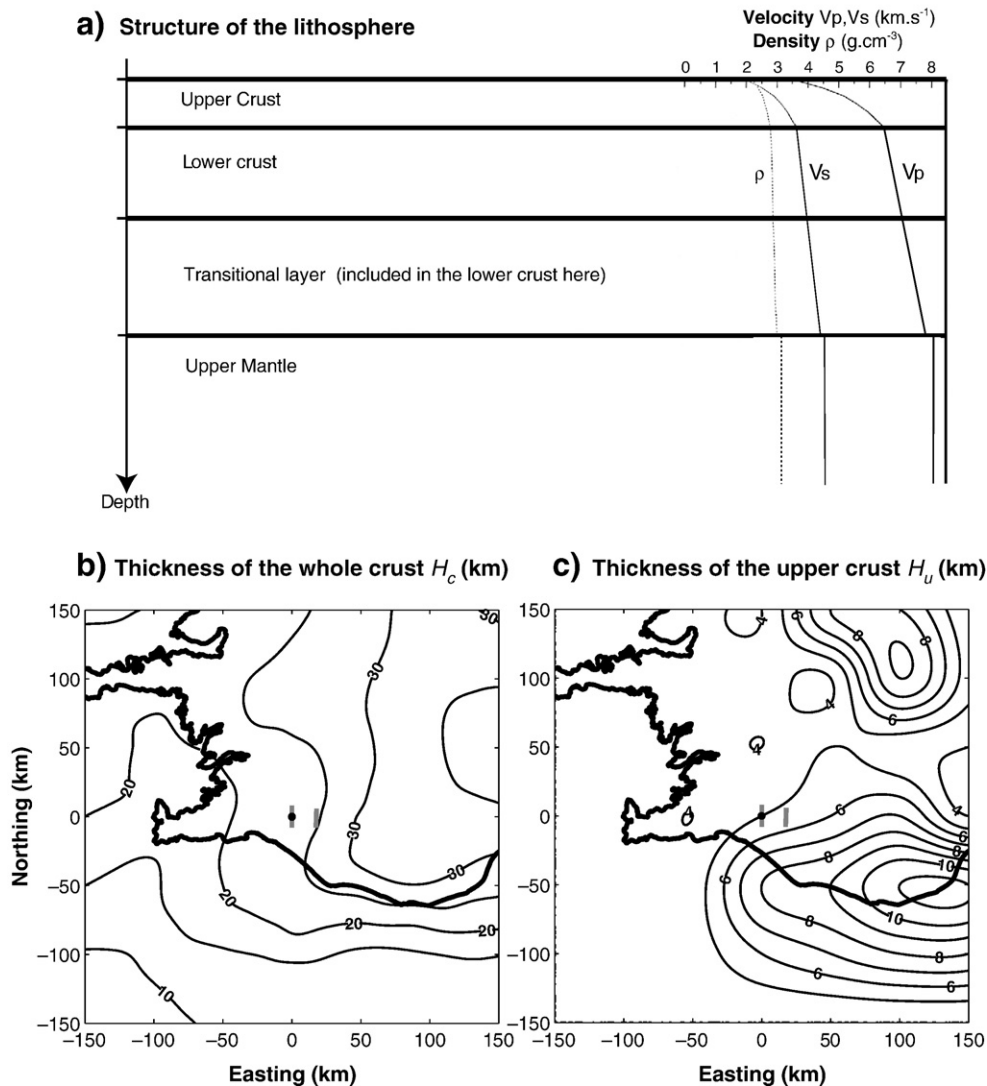


Fig. 3. (a) Typical structure of the Icelandic lithosphere including the main features found in the literature (Pálmason, 1971; Gebrande et al., 1980; Flóvenz and Gunnarsson, 1991; Bjarnason et al., 1993b; Menke et al., 1996; Staples et al., 1997; Darbyshire et al., 1998; Menke et al., 1998; Du and Foulger, 2001; Weir et al., 2001; Allen et al., 2002; Foulger et al., 2003). The layer with P-wave velocity between 7 and 8 km s⁻¹ is a subject of discussion. Here, it is considered as part of the lower crust. The solid lines correspond to the P- and S-wave velocities, and the dashed line, to the density (Bjarnason et al., 1993b; Árnadóttir and Olsen, 2000). (b) Depth of the interface between lower crust and upper mantle H_c (Kaban et al., 2002) implemented in the “Iceland” configuration. The contour interval is 5 km. (c) Thickness of the upper crust H_u (Darbyshire et al., 1998) as used in the “Iceland” configuration. The contour interval is 1 km. In (b) and (c), solid gray lines represent traces of modeled faults for June 17 (east) and June 21 (west). The black dot indicates the reference point of the local easting and northing coordinate system, located at (63.99°N; 20.71°W). It also corresponds to the center of the modeled June 21 dislocation, projected onto the surface.

an elastic lithospheric model: (1) a homogeneous configuration which is an elastic homogeneous medium, (2) a configuration which includes horizontal layers and a depth-dependent gradient in rigidity, (3) a configuration similar to the previous one (2) but in which the layers have variable thickness, introducing horizontal gradients in the rigidity (called the “Iceland” configuration), (4) a configuration adding weak fault zones (with lower rigidity) to the homogeneous configuration (1), and (5) a configuration adding weak fault zones (with lower rigidity) to the configuration with horizontal layers (2).

The first three configurations are also used in a visco-elastic model to study the influence of heterogeneities on post-seismic deformation. We describe the geometry and the rheology of these configurations below.

3.1. Geometry

The internal structure of Iceland (Fig. 3a) includes a thin upper crust with a strong gradient in seismic velocities (P-wave velocity ranging between 3.0 km/s and 6.5 km/s), overlying a thicker lower crust characterized by a very weak gradient for the seismic velocities (P-wave velocity ranging between 6.5 km/s and 7.0 km/s) (Pálmason, 1971; Gebrande et al., 1980; Flóvenz and Gunnarsson, 1991; Bjarnason et al., 1993b; Menke et al., 1996; Staples et al., 1997; Darbyshire et al., 1998; Menke et al., 1998; Du and Foulger, 2001; Weir et al., 2001; Allen et al., 2002; Foulger et al., 2003). Both these layers lie above a layer with P-wave velocity typically between 7.0 and 7.4 km/s that acts as a transitional layer between the crust and the mantle (Kaban et al., 2002). Below this transitional layer, the upper mantle is characterized by a P-wave velocity of about 8.0 km/s. In addition to seismic data, gravity data have been used to make structural interpretations (Staples et al., 1997; Menke, 1999; Darbyshire et al., 2000; Weir et al., 2001; Allen et al., 2002; Kaban et al., 2002). All these studies enable us to constrain the crustal thickness H_c in the “Iceland” configuration. This crustal thickness varies between approximately 20 km along the coast and 40 km under the Vatnajökull ice cap in the southeast part of Iceland (Fig. 3b). The upper crust is thinner, with a thickness H_u ranging from 7–8 km to 3–4 km under the active zones of the island (Fig. 3c). In the case of a horizontally-layered configuration, we assume that the values of H_u and H_c are roughly constant and equal to 5 km and 23 km, respectively, corresponding to the values under a point midway between the June 17 and June 21 faults.

Next, we specify the geometry of the two faults used in the elastic and visco-elastic models. The sensitivity analysis of Dubois (2006) shows that the surface deformation is less sensitive to the geometric fault parameters than to the rheologic parameters (especially in the upper crust). Indeed, the errors in the estimation of the geometric fault parameters are smaller than the 95% confidence intervals for this sensitivity study. We can therefore set the values of these geometric parameters to the values determined by Pedersen et al. (2003), without significantly changing our results. The faults are modeled as rectangular patches with right-lateral horizontal strike slip, which is free to reach the surface. The strike and the dip of the June 17 plane are fixed to 1.68°E and 87° to the east, respectively. A vertical plane with a strike of 0.5°E describes the June 21 fault. The length and the width of the faults are set to 23 km and 15 km respectively. These dimensions are larger than those used by Pedersen et al. (2003) to allow deeper and wider slip distributions in our heterogeneous configurations. The centers of the surface traces of the fault planes are located at 63.99°N; 20.71°W for the June 21 fault and at 63.99°N; 20.35°W for the June 17 fault. We use the latter point as the origin of our local coordinate system.

3.2. Rheology

The homogeneous configuration is similar to the model used by Pedersen et al. (2003). It is a homogeneous elastic medium with a

density ρ of 3000 kg m⁻³ and a rigidity μ of 30 GPa (Fig. 4). The Poisson's ratio ν is set to 0.28 (Jónsson et al., 2003; Pedersen et al., 2003).

In the other configurations, the values of the elastic parameters shown in Fig. 4 are calculated from the P- and S-wave velocities V_p and V_s as well as from the density ρ (Fig. 3a) under the SISZ as inferred by the SIL (South Iceland Lowland) project (Bjarnason et al., 1993b). We calculate the rigidity and Poisson's ratio using

$$V_p = \sqrt{\frac{2\mu(1-\nu)}{\rho(1-2\nu)}}, \quad V_s = \sqrt{\frac{\mu}{\rho}} \quad (1)$$

From these relations (1), we approximate the upper crust in the configuration with horizontal layers as five layers with a Poisson's ratio ν of 0.28 and a shear modulus μ ranging from 12 to 34 GPa. Each layer has a thickness of 1 km. The stiffness in this configuration thus increases with depth, following the steep gradient in seismic velocity. Since this gradient is less steep below, we can describe the lower crust with only two layers. Each layer has a thickness of 9 km, a Poisson's ratio ν of 0.25, and a shear modulus μ from 40 to 45 GPa. At the bottom of the configuration, the mantle is homogeneous with a Poisson's ratio ν of 0.30 and a shear modulus μ of 60 GPa.

The configurations with fault damage zones are similar to the homogeneous configuration and to the one with horizontal layers. The only difference is a low-rigidity zone centered on the faults to describe the damaged rocks near them. According to Cocco and Rice (2002, 2003), the shear modulus μ in this fault damage zone is typically four times smaller than in the surrounding rocks, assuming that the density ρ and the bulk modulus K are the same. Therefore, the shear modulus μ in the homogeneous configuration with fault damage zones is around 7.5 GPa in each fault zone, which we assume to be a box of 600 m width, centered on the fault and with a depth extending to the bottom of the mesh. In the horizontally-layered configuration with fault damage zones, these zones are geometrically similar except for their depths, which correspond to the bottom edge of the modeled fault. We assume that only the uppermost layer has its shear modulus μ lowered by a factor of four and that this parameter increases linearly with depth in the fault damage zones (Fig. 4). This simple assumption is a first step toward accounting for a reduction in damage with depth because of stiffer rigidity. In these configurations, the Poisson's ratio ν in the fault damage zones is obtained from the relations (1) using the reduced values of shear modulus μ .

The rheology of the “Iceland” configuration is identical to that of the model with horizontal layers (Fig. 4). Only the geometry of the upper and lower crust is different, allowing us to model the dip toward the east across the SISZ for these two layers (see Section 3.1 and also Fig. 3b and c) as observed in previous three-dimensional studies (Darbyshire et al., 2000; Allen et al., 2002; Kaban et al., 2002).

The visco-elastic model is based on the configurations without fault damage zones, but with the same elastic properties. The goal of this visco-elastic modeling is to estimate the sensitivity of viscous deformation to two kinds of heterogeneities: the vertical gradient of increasing rigidity and the horizontal gradients in both rigidity and viscosity due to the geometry of the upper and lower crust. Here we do not discuss the effect of gravity or the influence of elastic thickness, which have been described elsewhere (Rundle, 1982; Fernández et al., 1996; Wang et al., 2006). The literature gives a wide range of values for the thickness of this layer. For example, Kaban et al. (2002) find a value of 6 km whereas other authors estimate the elastic thickness to be around 10 km (Hackman et al., 1990; Pollitz and Sacks, 1996; Tryggvason et al., 2002) or 20 km (Sigmundsson, 1991; Sigmundsson and Einarsson, 1992; Thoma and Wolf, 2001). Here we choose to model the extreme case (smallest elastic thickness) and therefore introduce two values for the linear Maxwell viscosity, one in the lower crust and another in the upper mantle,

Depth	homogeneous configuration			horizontally-layered & Iceland configurations			homogeneous configuration (in fault damage zones)			horizontally-layered configuration (in fault damage zones)		
	ρ	μ	ν	ρ	μ	ν	ρ	μ	ν	ρ	μ	ν
Surface	3000	30	0.28	2306	12.2	0.28	3000	7.5	0.44	2306	3.1	0.44
$-H_u/5$				2512	19					2512	5.6	0.43
$-2 \times H_u/5$				2630	25.6					2630	8.7	0.42
$-3 \times H_u/5$				2706	30					2706	11.6	0.41
$-4 \times H_u/5$				2753	34.3					2753	14.8	0.40
$-H_u$				2830	41.3	0.25				2830	26.3	0.33
$-(H_c + H_u)/2$				2959	45					2959	45	0.25
$-H_c$				3322	60	0.30				3322	60	0.30

- - - - Density ρ (kg.m⁻³) ——— Rigidity μ (GPa) ——— Poisson's ratio ν

Fig. 4. Cross section showing rheologic parameters as a function of depth: density ρ (thick dashed line), rigidity μ (thick solid line), and Poisson's ratio ν (thin solid line). The thicknesses of the rheologic layers depend on H_u and H_c , the depths to the bottoms of the upper and lower crustal layers, respectively (see Section 3.1). The configurations are: a uniform half-space (homogeneous configuration), horizontal layers with constant thickness which enable vertical gradients of elastic parameters (horizontally-layered configuration), dipping layers with variable thickness which enable vertical and horizontal gradients of elastic parameters ("Iceland" configuration), a half-space with fault damage zones (homogeneous configuration with fault damage zones), and horizontal layers with fault damage zones (horizontally-layered configuration with fault damage zones).

whereas the upper crust remains elastic, as in [Kaban et al. \(2002\)](#). The density ([Fig. 4](#)) is used only to calculate the elastic parameters based on the relations (1). The viscosity for the elements in the ductile lower crust

and upper mantle is set to 10^{19} Pa s ([Dubois, 2006](#)), which is compatible with the results of [Sigmundsson and Einarsson \(1992\)](#), [Pollitz and Sacks \(1996\)](#), and [Árnadóttir et al. \(2005\)](#).

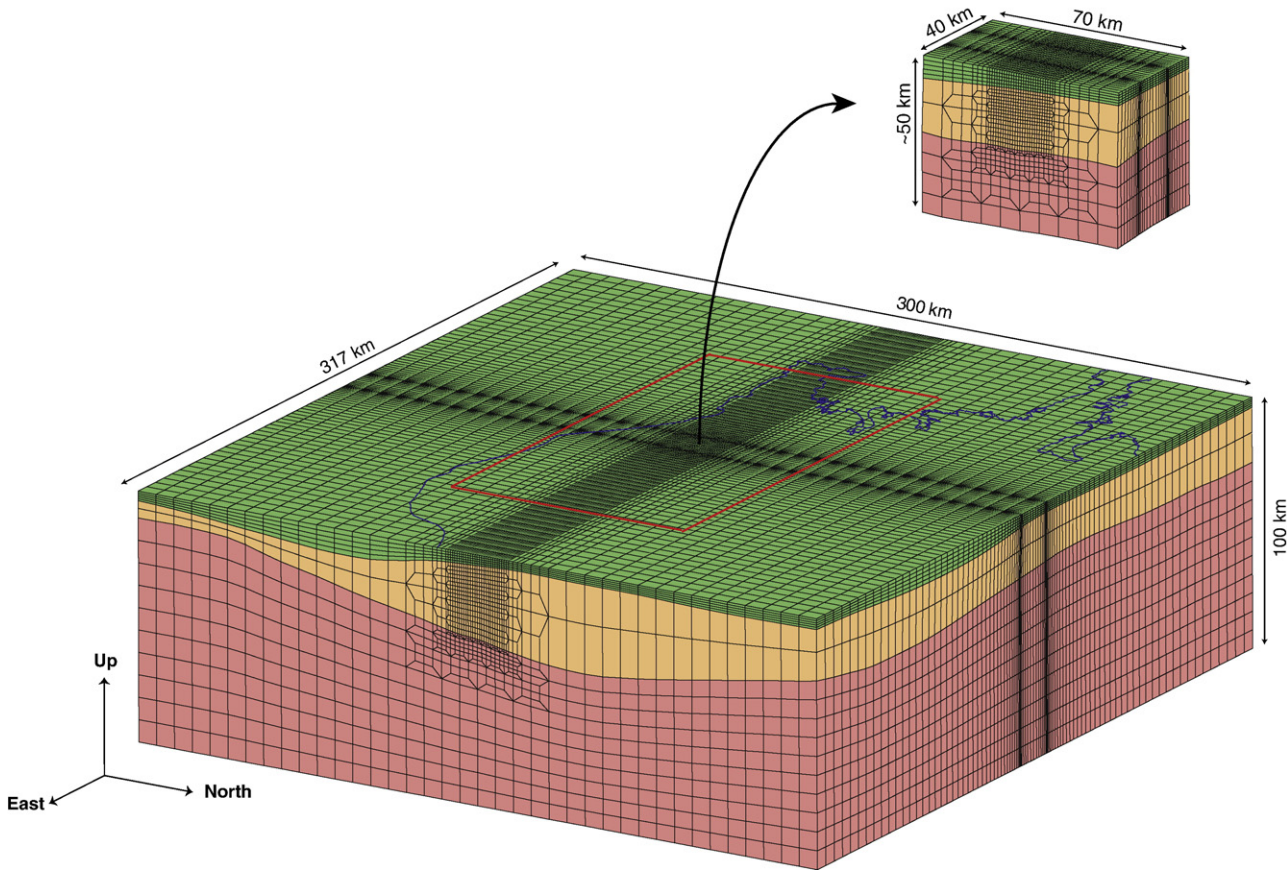


Fig. 5. "Variable" mesh used with the "Iceland" configuration and modeling thickening of the crust from east to west across the SISZ. The dimensions of the mesh are 317×300×100 km (whole box). The color code shows the Icelandic coast (blue line), the 180×100 km studied zone (red rectangle), the upper crust (green), the lower crust (orange), and part of the upper mantle (red). The coordinates are easting, northing and upward components of position with respect to a reference point located at the center of the modeled June 21 fault trace (63.99°N, 20.71°W) and shown by a gray dot in [Fig. 3b](#) and [c](#). Note that the mesh is denser near the modeled dislocations. The "horizontal" mesh is similar but with upper/lower crust and crust/mantle interfaces that are horizontal ($H_u=5$ km and $H_c=23$ km).

4. Methods

4.1. Finite-element method (FEM)

To calculate the surface displacements due to slip in the fault plane, we use TECTON (Williams and Richardson, 1991), a software package that implements a finite-element formulation based on three-dimensional hexahedral elements. A revised version of this package, now called PyLith/LithoMop, is maintained by the Computational Infrastructure for Geodynamics (CIG, 2008). We have created two meshes (Fig. 5) to account for the primary interfaces in our problem: upper/lower crust, mantle/crust, as well as the fault rupture planes for the June 17 and June 21 mainshocks. The mesh for the homogeneous configuration, also used for the horizontally layered configuration and both configurations with fault damage zones, includes horizontal layers with constant thickness (labeled “horizontal” mesh). A different mesh (labeled “variable” mesh and shown in Fig. 5) is used for the “Iceland” configuration. To increase our confidence in the solutions calculated with this configuration, we test the “horizontal” and “variable” meshes with a homogeneous distribution of elastic parameters. The co-seismic surface displacement fields calculated using these two meshes differ by less than 0.1 mm for all three components (see the elastic TECTON test below). Thus the error introduced by comparing solutions from two different meshes is negligible.

For both meshes, the boundary conditions on the bottom and four vertical sides are fixed to have zero displacement while the top surface is free to move. The region under study has a size of 180 km by 100 km by 30 km. Its surface projection is shown by a red box in Fig. 5. To avoid edge effects, we extend the meshes to a larger region of 317 km by 300 km by 100 km. The elastic solution achieves numerical convergence with a 3D mesh of approximately 70,000 nodes (Dubois, 2006), but we use 140,000 nodes in order to have a regular grid of nodes with a resolution of 1 km for the modeled dislocations related to the June 17 and June 21 events. The fault slips are described as relative horizontal displacements at 690 so-called “split nodes” (Melosh and Raefsky, 1981) that permit discontinuities in the model. The convergence of the visco-elastic solution is obtained with a gradual time step calculation as described by Dubois (2006). In the beginning, the time step is one tenth of the smallest Maxwell time τ_M . Later, it is equal to $5\tau_M$ near complete relaxation after $50\tau_M$.

To evaluate the accuracy of the elastic TECTON solution in the case of our models, we compare its predictions to the analytical solution for a rectangular dislocation buried in an elastic half-space formulated by Okada (1985) and implemented in the RNGCHN code of Feigl and Dupré (1999). Using a dislocation with a homogeneous slip distribution equivalent to an $M_w=7$ earthquake, we calculate the displacement field at the surface using both methods. The average difference is less than 1 mm in all three components, thus validating our finite-element approach in the elastic case (Dubois, 2006).

For the post-seismic visco-elastic models, we compare the surface displacement fields calculated using two different methods: first our finite-element approach using the TECTON software, as described above, and second a semi-analytical Green's function approach using the PSGRN/PSCMP software of Wang et al. (2006). The average difference in surface displacement is less than 3 mm for all three components after complete relaxation, thus validating our finite-element approach in the visco-elastic case (Dubois, 2006).

4.2. Co-seismic joint inversion

To estimate the distribution of slip on the June 17 and June 21 fault planes, we use the same data set and inversion algorithm as Pedersen et al. (2003). The latter is a damped non-negative least squares algorithm (Lawson and Hanson, 1974). Pedersen et al. (2003) have used the

Okada (1985) analytical formulation to calculate the elastic Green's functions, i.e. the partial derivatives of the measurable quantities (displacements) with respect to the model parameters (slip on discrete fault patches). Pedersen et al. (2003) were limited to a homogeneous half-space model with this method. In this study, we want to investigate the influence of rheologic and geometric heterogeneities on slip estimates. We therefore use the three-dimensional FEM formulation to calculate the elastic Green's functions. This difference in approach entails a difference in the fault parameterization. The analytical dislocation formulation specifies the slip as a constant value inside each rectangular rupture patch on the fault plane. The parameterization in the finite-element approach assigns a slip value to each *split node*. In other words, the slip distribution is discontinuous in the dislocation formulation, but continuous (piece-wise planar) in the finite-element formulation. As a result, the latter leads to smoother slip distributions and smaller stress concentrations than the former.

The system of equations that we have to invert has the following form:

$$\begin{bmatrix} \mathbf{C}_d^{-1/2} \mathbf{d}_{\text{obs}} \\ 0 \end{bmatrix} = \begin{bmatrix} \mathbf{C}_d^{-1/2} \mathbf{K}_g \\ \kappa \mathbf{L} \end{bmatrix} \mathbf{m} \quad (2)$$

where \mathbf{d}_{obs} is a vector containing the data (data vector with the 582 InSAR points and the 3×37 GPS components), \mathbf{C}_d is the covariance matrix of the data, \mathbf{K}_g is the kernel constructed with the Green's functions, κ the smoothing parameter, \mathbf{L} the discrete Laplacian operator and \mathbf{m} is a vector of model parameters with the slip value of each split node. The non-negative least squares inversion of system (2) enables us to calculate the slip distribution \mathbf{m}_{cal} (“cal” for calculated).

To evaluate the uncertainty of the slip distribution calculation, we apply the posterior covariance operator described by Tarantola (2005). We obtain only a rough estimate of this uncertainty because this operator is not well defined for an inversion with a non-negative least squares algorithm. A more rigorous method is to use a bootstrap algorithm (Efron and Tibshirani, 1986). Accordingly, we resample $N_b=1000$ times the data vector randomly according to its (diagonal) covariance. For each realization of the data vector, we solve the inverse problem to find a population of the estimates \mathbf{m} for the model parameters \mathbf{m} . The standard deviations of the model parameter estimates are then

$$\sigma(\mathbf{m}) = \sqrt{\frac{\sum_{i=1}^{N_b} [\hat{\mathbf{m}}_i - E(\hat{\mathbf{m}})]^2}{N_b - 1}} \quad (3)$$

where the E operator denotes the expected value. However, this method gives an uncertainty value that is too optimistic (low) because it neglects model uncertainty. The geometric contribution of the relative positions of the data points and the modeled faults is not accurately evaluated. The uncertainties that we show are the maximum values obtained from the two methods. We therefore have a pessimistic estimate of the accuracy of our inversion.

In our inversion, we must choose the appropriate amount of smoothing to optimize the trade-off between fitting the data (RMS misfit) and finding a slip distribution with a physically plausible roughness

$$R = \|\mathbf{L}\mathbf{m}_{\text{cal}}\|_1. \quad (4)$$

Here we choose the value of the smoothing parameter by applying the geometric smoothing optimization criterion described by Freymueller et al. (1994). This value ($\kappa=0.4$) is the same for all configurations (Fig. 6) and is different from the one used by Pedersen et al. (2003) because of the difference between our modeling approach (split nodes) and theirs (fault patches).

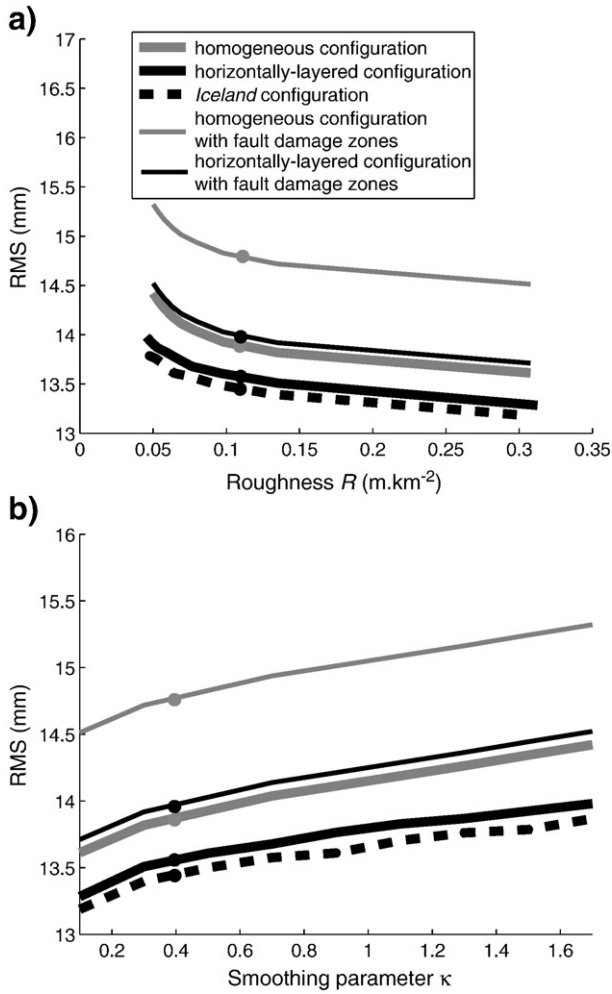


Fig. 6. (a) Trade-off between the misfit (residual RMS) and the smoothing efficiency (roughness R). (b) Relation between the inversion efficiency (RMS) and the smoothing parameter κ . The optimized value for κ (circles) is chosen from the trade-off curve in panel (a) using the geometric method described by Freymueller et al. (1994). The chosen value corresponds to $\kappa=0.4$ in (b).

4.3. Stress changes

Next, we evaluate the stress contributed by several processes observed in the SISZ. As described in the Introduction, there are five processes, not counting seismic waves. For each process, we calculate the Coulomb stress changes in the SISZ using the following relation (Rice and Cleary, 1976)

$$\Delta\sigma_c = \Delta\sigma_t + \mu_f \left(\Delta\sigma_n - \frac{B}{3} \Delta\sigma_{kk} \right) \quad (5)$$

where B is Skempton's coefficient, μ_f is the coefficient of friction on the "receiver" fault, $\Delta\sigma_t$ is the change in shear stress projected onto the "receiver" fault plane (taken positive in the sense of the slip vector), $\Delta\sigma_n$ is the change in normal stress (taken positive in tension), and σ_{kk} is the trace of the stress tensor. Using the Coulomb failure stress relation with the effective coefficient of friction (Rice and Cleary, 1976) does not alter our conclusions. To evaluate the Coulomb failure stress changes, we project the tensor of stress changes onto a right-lateral strike-slip vector lying with a north-striking vertical "receiver" fault plane that typifies the SISZ focal mechanisms (Árnadóttir et al., 2003; Dubois, 2006). The result is a scalar Coulomb stress change $\Delta\sigma_c$. Following a previous study in the area (Árnadóttir et al., 2003), we set

$B=0.5$ and $\mu_f=0.75$. The sensitivity of the stress changes to modifications in these coefficients has been evaluated in previous studies (King et al., 1994; Cocco and Rice, 2002, 2003). We have not attempted to adjust B or μ_f because King et al. (1994) found that "any improvements to the correlation between stress changes and aftershock occurrence are modest".

First, we estimate the influence of the elastic lithospheric model on the stress changes. The slip distribution estimated for each configuration is used to calculate the co-seismic Coulomb failure stress changes related to the June 17 mainshock.

Second, the visco-elastic contribution of both June 2000 earthquakes is calculated with a viscosity value of 10^{19} Pa s for the upper mantle and the lower crust. The calculation is performed for each configuration of the visco-elastic model to qualitatively evaluate the sensitivity of the stress changes to the heterogeneities incorporated in our modeled lithosphere (e.g., layering and variable thickness of the crust).

Third, we estimate the complete poro-elastic contribution of the June 17 earthquake in the case of the horizontally-layered configuration. We employ a modeling approach, originally introduced by Rice and Cleary (1976), which assumes a change in elastic properties, specifically Poisson's ratio, from an undrained state (fluids with the solid matrix resist instantaneous co-seismic deformation) to a completely drained state (fluids are free to flow and only the solid matrix resists long-term deformation), also employed by other authors for several other earthquakes in different tectonic settings (Peltzer et al., 1998; Fialko, 2004). In practice, we run TECTON twice with the horizontally-layered configuration and with the slip distribution estimated from the co-seismic inversion: the first time in an undrained state (rheologic parameters shown in Fig. 4) and the second time in a drained state by assuming a decrease of $\Delta\nu=0.06$ in Poisson's ratio that is similar to the model of Jónsson et al. (2003). The complete poro-elastic displacement field is deduced by subtracting the field obtained with the drained state from the one calculated with the undrained state. The validity of the assumptions underlying this simple, static and elastic approximation to what is actually a complex, time-dependent, poro-elastic problem (Wang, 2000) will enter into our discussion below.

We then evaluate the influence of seismicity during the time interval from the June 17 earthquake to December 31, 2000, excluding the June 21 mainshock. The data set compiled by the SIL network (Stefánsson et al., 1993; Bödvarsson et al., 1999) gives the location and the focal mechanism for each of the 14,388 earthquakes having a magnitude $M_w \geq 0$. To account for the effects of the micro-seismicity, we estimate the stress changes produced by all these events in the configuration with horizontal layers by using the semi-analytical EDGRN/EDCMP code (Wang et al., 2003) to save computation time. In this calculation, we consider the events with $M_w < 4.8$ as point sources. The other events are modeled as rectangular dislocations with a length equal to 1.5 times their width (Wells and Coppersmith, 1994).

Finally, we evaluate the usefulness of building further complex geometric and rheologic models to study inter-seismic deformation. We run simple models with TECTON to calculate the stress changes over 100 years of strain accumulation in the SISZ to test if the eastward thickening of the crust can produce an asymmetric stress distribution. These models are derived from the horizontally layered and "Iceland" configurations of the elastic lithospheric model by removing both co-seismic dislocations and by applying a velocity of 0.95 cm yr^{-1} in the $N110^\circ E$ direction as a boundary condition on the North American and Eurasian faces of the mesh (DeMets et al., 1990, 1994). The meshes are similar to the "horizontal" and "variable" meshes (see Section 3 and also Fig. 5) but slightly modified to have two opposite lateral sides perpendicular to the stretching direction. To compute the stress changes produced by the geometric variation in crustal thickness, we run this model twice, once in the configuration with horizontal layers, and then in the "Iceland" configuration with crust thickening toward the east. After projecting the resulting stress changes onto North-striking vertical strike-slip faults, we subtract the two fields to

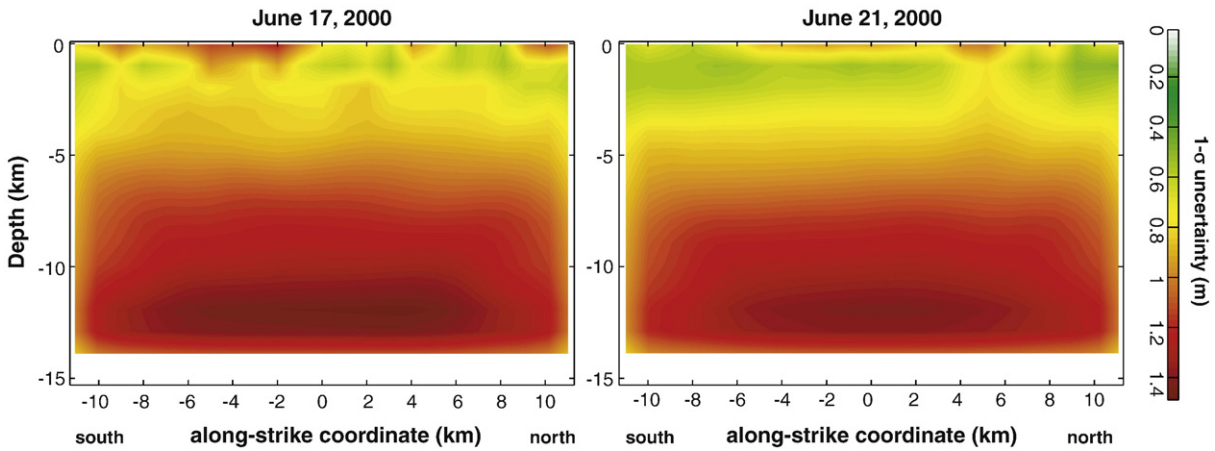


Fig. 7. View of fault planes showing the estimate for the 1- σ uncertainty of the calculated slip for the June 17 (left) and June 21 (right) events.

obtain the geometric contribution to the changes in Coulomb failure stress.

5. Results

5.1. Co-seismic joint inversion

The results of the inversions in all the configurations fit the data as well as those in Pedersen et al. (2003) (Fig. 6). The “Iceland”

configuration has the best fit but its RMS misfit is not significantly better than for the other configurations. Fig. 2c and d shows the interferometric residuals and Fig. 2e and f shows maps with the modeled displacements and the GPS measurements. Although these maps have been calculated using the configuration with horizontal layers, the other configurations yield similar results (Dubois, 2006). In the residual interferogram for T95, the same signal near the June 17 fault appears for each configuration, confirming that it is not an artifact. This signal has been interpreted as poro-elastic deformation (Jónsson et al., 2003).

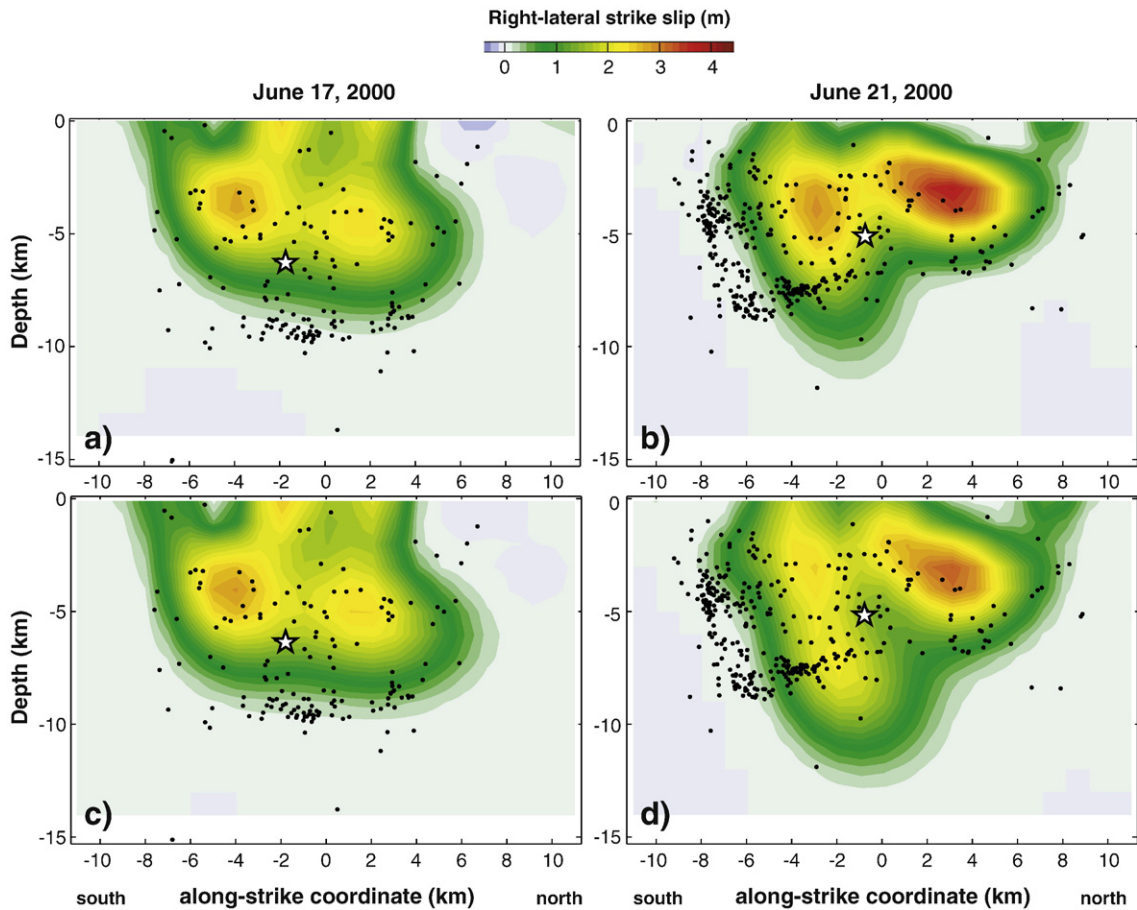


Fig. 8. View of fault planes showing the slip distribution estimated for the June 17 mainshock (left column) and June 21 mainshock (right column) in the homogeneous (upper row) and horizontally layered (lower row) configurations. The white stars indicate the hypocenters of the mainshocks. The black dots indicate aftershocks within 1 km of each fault and 24 h of the June 17 and June 21 mainshocks, respectively. These aftershocks have been relocated by the Icelandic Meteorological Office (IMO, 2006), as described in Section 2.

The uncertainty in the calculated slip distribution (Fig. 7) reaches more than 1 m near the surface, particularly in the section of the June 17 fault south of the hypocenter. This result may reflect discrepancies between the InSAR and GPS measurements at locations near the fault. Elsewhere on both faults, the standard deviation of the slip is less than 0.5 m as deep as 5 km depth and increases to about 1.4 m below 12 km depth. This pattern is consistent with previous studies. The resolution is better in the uppermost 5 km and degrades with depth below (Pedersen et al., 2003).

Using the homogeneous configuration, we have estimated the distribution of co-seismic slip on the June 17 and June 21 fault planes (Fig. 8a and b). It is similar to that estimated using the fault patch parameterization (Pedersen et al., 2003), further validating our finite-element approach. Most of the slip is shallow, above 6 km depth. The

slip decays to less than 0.5 m below 9 km depth for the June 17 fault and below 11 km depth for the June 21 fault. The centroid depths are 3.7 and 3.8 km, respectively. Some of the aftershock hypocenters are located outside the high-slip areas: between 8 and 10 km depth in the June 17 fault plane and between easting coordinates -8 and -6 km in the June 21 fault plane.

Fig. 8c and d shows the slip distribution estimated using the configuration with horizontal layers. The differences between the horizontally layered and homogeneous configurations appear in Fig. 9a and b. The slip extends slightly deeper in the horizontally-layered configuration than in the homogeneous one. The centroid is located 0.3 km deeper for the June 17 fault and 0.5 km deeper for the June 21 fault. For the June 21 fault, there is a zone with about 1 m more slip at 10 km depth in the horizontally-layered

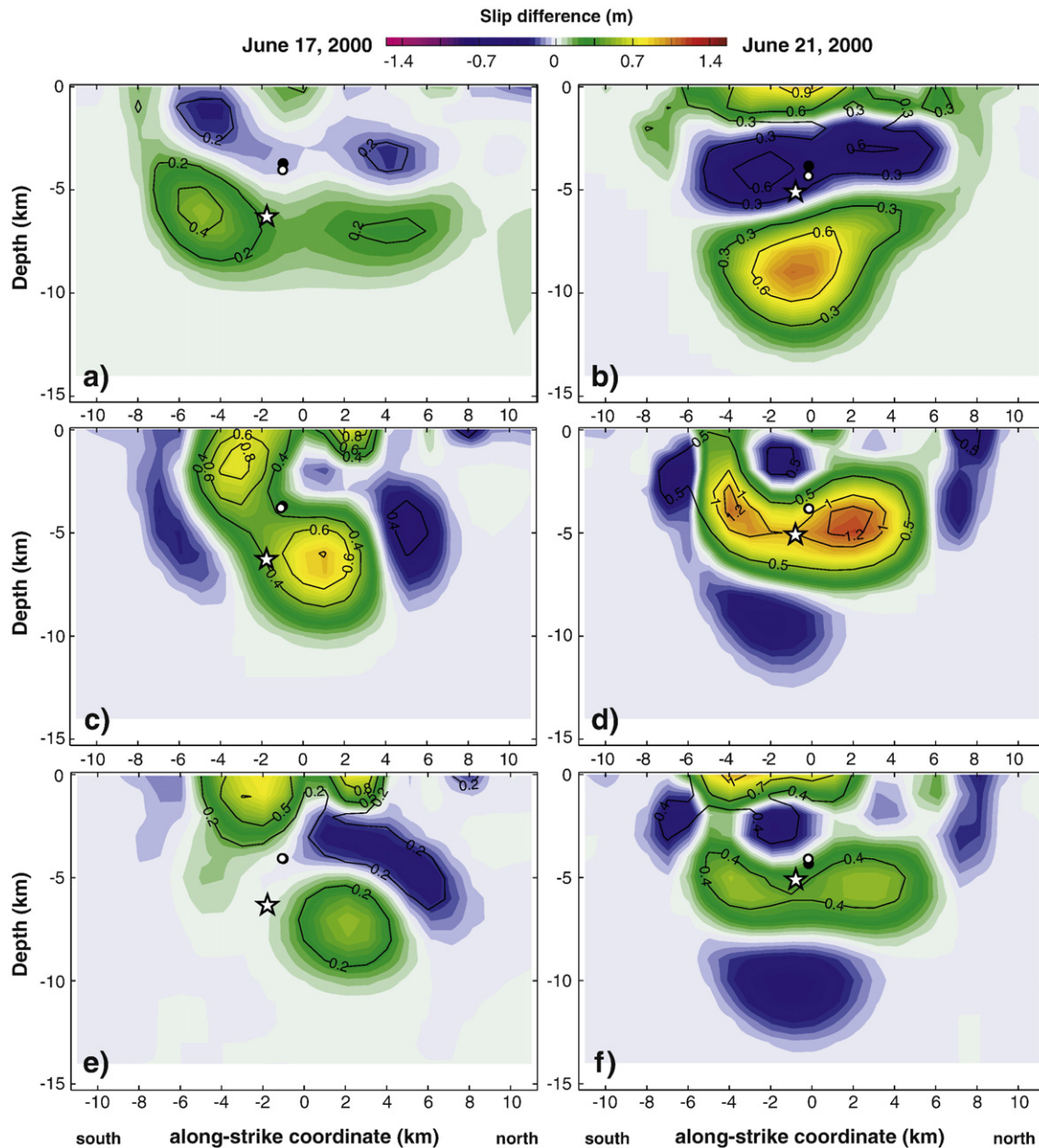


Fig. 9. View of fault planes of the June 17 mainshock (left column) and June 21 mainshock (right column) showing the differences in estimated slip distribution for the horizontally-layered configuration with respect to the homogeneous one (top row), the homogeneous configuration with fault damage zones with respect to the homogeneous one (middle row), and the horizontally layered configuration with fault damage zones with respect to the horizontally layered one (bottom row). The black lines denote the significance ratio, defined as the differences in the slip estimates divided by their $1-\sigma$ uncertainties (Fig. 7). The contour where this ratio equals 1 thus includes the area where the differences are statistically significant at the 68% confidence level. For each panel, the white circle indicates the centroid of the first slip distribution in the pair, while the black circle indicates the centroid of the second, e.g., the white circle is the centroid for the horizontally-layered configuration in the first row. The white stars indicate the hypocenters of the mainshocks.

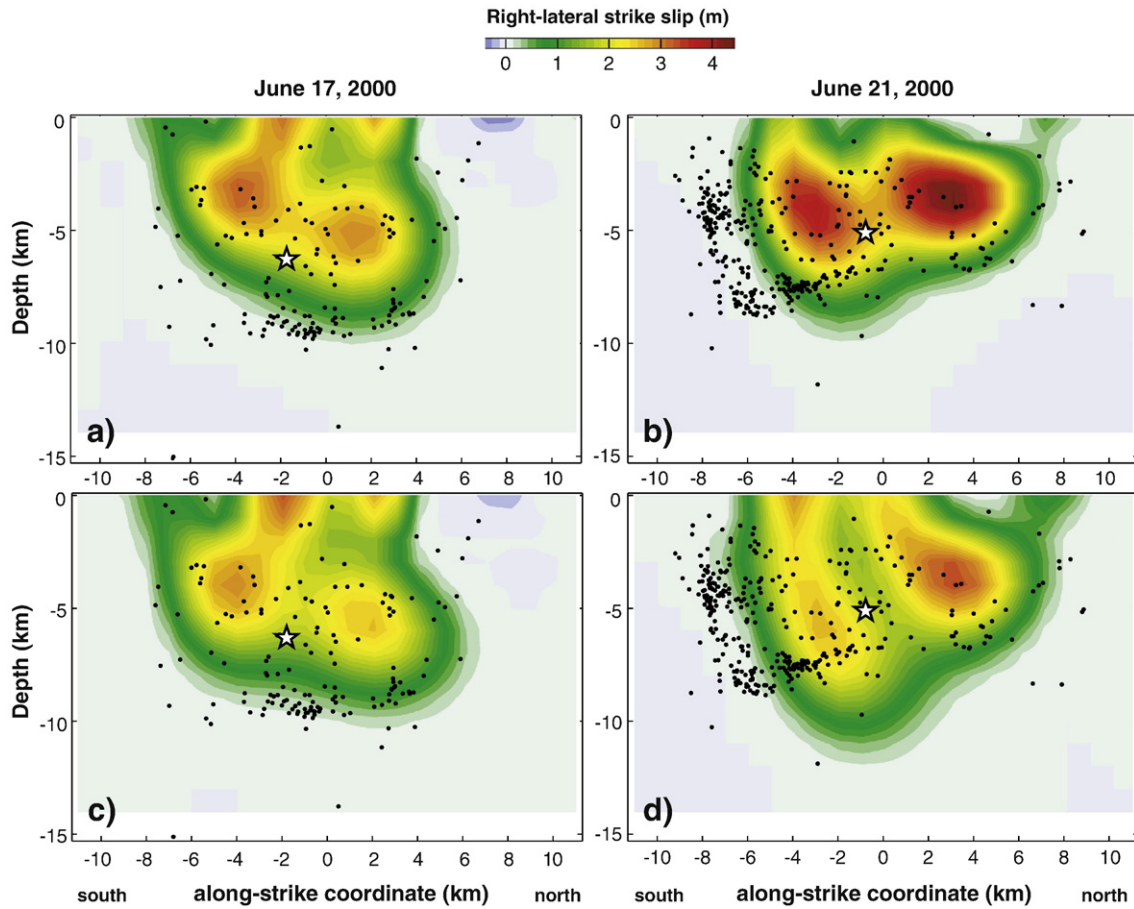


Fig. 10. Views of the fault planes showing the slip distribution estimated for the June 17 mainshock (left column) and June 21 mainshock (right column) in the homogeneous (upper row) and horizontally-layered (lower row) configurations with fault damage zones. The white stars indicate the hypocenters of the mainshocks and the black dots indicate aftershocks within 1 km of each fault and 24 h of the June 17 and June 21 mainshocks, respectively. These aftershocks have been relocated by the Icelandic Meteorological Office (IMO, 2006), as described in Section 2.

configuration than in the homogeneous configuration. The increase in slip concentrates around the hypocenter relocated at 5.1 km depth from seismology using a layered velocity model (Árnadóttir et al., 2001). This difference (Fig. 9b) is statistically significant if we remember that the standard deviation of the estimate in the configuration with horizontal layers is pessimistic (Fig. 7). The slip estimated at the surface is also significantly larger when calculated in the horizontally-layered configuration than in the homogeneous configuration. The slip distributions using the “Iceland” configuration are essentially the same as those found in the configuration with horizontal layers (Dubois, 2006).

The slip estimated in the homogeneous configuration with fault damage zones (Fig. 10a and b) concentrates in the upper crust, significantly increasing the maximum slip value around the June 21 hypocenter at 5 km depth (Fig. 9d). For the June 17 fault plane, the slip is significantly shallower in the distribution with this configuration than in the one with the homogeneous configuration. Of all the configurations, the homogeneous one with fault damage zones exhibits the steepest slip gradient and thus the highest residual stress. The aftershock locations appear to correlate with these areas of high high-slip gradients, particularly for the southern edge of the June 21 rupture. Adding a fault damage zone to the heterogeneous configurations also changes the slip distribution. The result with the horizontally-layered configuration with fault damage zones (Fig. 10c and d) has significantly more slip in the uppermost mesh elements and around the hypocenters in both fault planes (Fig. 9e and f).

The magnitudes estimated in configurations that include the heterogeneities of each configuration are quite similar, with a value of about $M_w=6.5$, except for the configurations with fault damage zones, which give lower values: $M_w=6.1$ for the homogeneous configuration with fault damage zones and $M_w=6.3$ for the horizontally-layered configuration with fault damage zones. Although the damage zones show large amounts of slip, they contribute little to the seismic moment (and magnitude) because the shear modulus is low in them. However, the modeling of a fault damage zone is not well constrained in our study, as noted above.

5.2. Stress changes

The vertical lithospheric heterogeneities have a clear influence on the co-seismic stress changes caused by the June 17 earthquake (Fig. 11a). In map view, the area within a contour of 10 kPa is somewhat smaller when calculated with the horizontally-layered configuration than with the homogeneous configuration. This effect is noticeable in the uppermost part of the crust and fades out below 10 km depth. Interestingly, the “Iceland” configuration with variable crustal thickness yields a Coulomb stress field that is slightly asymmetric compared to the result from the configuration with horizontal layers. Indeed, the lobe on the west side of the June 17 fault is about 4 km smaller than the one on the east side. This effect is not significant enough to explain the westward migration of seismicity across the SISZ.

The complete poro-elastic relaxation seems to contribute very little to the stress changes and only in a very small area (Fig. 11b). On

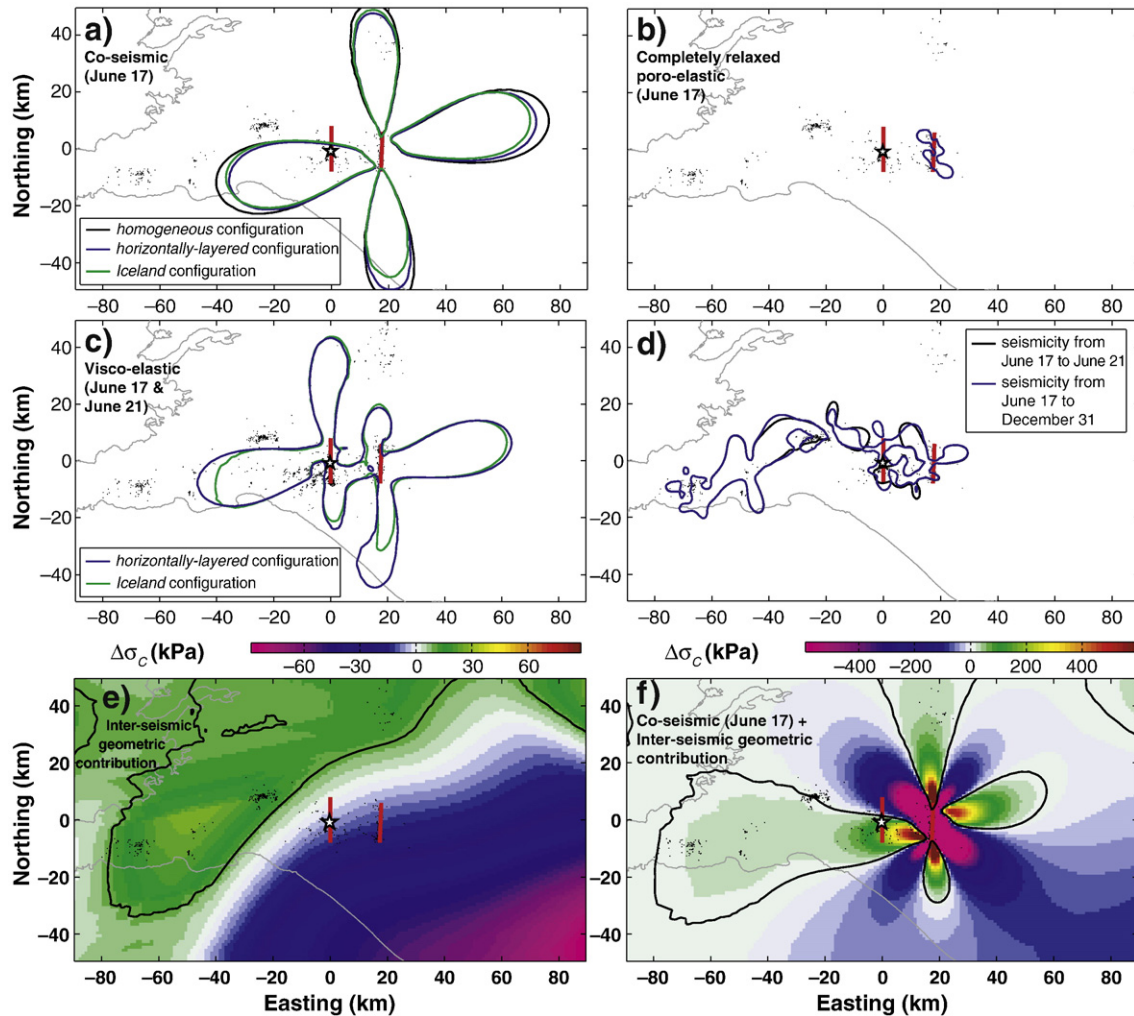


Fig. 11. Changes in Coulomb failure stress $\Delta\sigma_c$ as a result of five candidate processes. The contours outline the areas where the change in Coulomb failure stress $\Delta\sigma_c$ resolved on north-striking vertical faults at 4 km depth exceeds 10 kPa. Red lines indicate faults for the June 17 (east) and June 21 (west) mainshocks. The dots in panels (a, b, c, e, f) indicate the epicenters of earthquakes between June 17 and 21, 2000. The dots in panel (d) indicate the epicenters of earthquakes between June 17 and December 31, 2000 (Vogfjörd, 2003; Hjaltadóttir et al., 2005). The sources of stress include: (a) co-seismic stress changes generated by the June 17 mainshock calculated using the homogeneous (black line), horizontally-layered (blue line) and “Iceland” (green line) configurations; (b) poro-elastic effects calculated with the horizontally-layered configuration and using the elastic approximation of a complete relaxation with two different values of Poisson’s ratio n , as described by Jónsson et al. (2003); (c) visco-elastic relaxation over 4 years calculated with the horizontally-layered (blue line) and “Iceland” (green line) configurations; (d) “domino” effect of cascading aftershocks from June 17 to June 21, 2000 (black) and from June 17 to December 31, 2000 (blue) calculated by summing the co-seismic stress changes for all the aftershocks with magnitude greater than zero during these time intervals and excluding the two $M_w=6.5$ mainshocks; (e) geometric contribution to 100 years of inter-seismic strain accumulation obtained by subtracting the inter-seismic changes in the stress field calculated using the horizontally-layered configuration from that obtained with the “Iceland” configuration. (f) Combination of the co-seismic and the geometric contribution to the inter-seismic stress changes integrated over 100 years, calculated as the sum of the stresses shown in panels (a) and (e).

the other hand, after four years of post-seismic viscous relaxation, the Coulomb failure stress changes at 4 km depth are of the same order of magnitude as the static co-seismic stress changes caused by both June 2000 events. Moreover, Fig. 11c shows that the 10 kPa contour area for the “Iceland” configuration of the visco-elastic model is smaller than the area for the horizontally-layered configuration. The former has an asymmetric shape, highlighting the importance of a realistic geometric configuration in visco-elastic stress calculations. Dubois (2006) has shown that these results remain similar if we vary the viscosity values of the upper mantle and the lower crust in an interval compatible with the conclusions of previous studies (Sigmundsson and Einarsson, 1992; Pollitz and Sacks, 1996; Árnadóttir et al., 2005).

Fig. 11d shows the changes in static Coulomb failure stress at 4 km depth due to the seismicity that occurred 3.5 days and 6 months after the June 17 event (excluding the June 21 earthquake). These stress changes seem to have been caused mostly by some $M_w=5$ events. The

area inside the 10 kPa contour is approximately one fourth the size of that contributed by both June 2000 mainshocks. The small changes appearing after 6 months show that the other events with $M_w < 5$ have a small, but non-negligible influence. The surface deformation induced by seismicity (excluding both $M_w=6.5$ mainshocks) can involve displacements of about 3 cm at some locations (Dubois, 2006). If models do not take this displacement into account, then centimeter-scale errors can be introduced.

In our simple inter-seismic model, we have calculated the contribution of the eastward thickening to the stress changes caused by plate motion accumulating over 100 years, the typical recurrence time for large ($M > 6$) earthquakes in the SISZ. The resulting stress field exhibits a strong gradient, such that the stress is 10 to 40 kPa higher on the June 21 fault than on the June 17 fault (Fig. 11e). To account for this asymmetric effect in the June 2000 sequence, we combine the previous stress field with the co-seismic Coulomb failure stress changes produced by the June 17 mainshock alone (Fig. 11f). The result

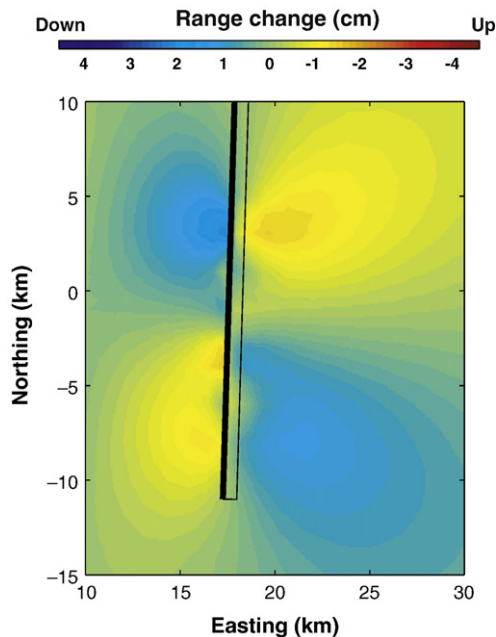


Fig. 12. Map view of range change (the component of displacement along the line of sight from the satellite to the ground) due to complete poro-elastic relaxation calculated using a ubiquitous value for the change of Poisson's ratio $\Delta n = 0.04$ in the homogeneous configuration. A negative range change corresponds to uplift and a positive range change corresponds to subsidence. Solid black lines outline the co-seismic portion of the fault plane that ruptured during the June 17 mainshock.

of this calculation exhibits an asymmetric distribution that could explain the westward migration of seismicity.

6. Discussion

6.1. Surface slip and poro-elastic relaxation

The co-seismic inversions in the layered configurations show more slip in the uppermost 2 km of the crust than those in the homogeneous half-space configurations (Fig. 9a and b). If we follow Jónsson et al. (2003) in assuming that poro-elastic stresses have completely relaxed within a month or two of the mainshock, we can use a single, ubiquitous value for the change in Poisson's ratio. This "completely relaxed" approximation has been described in Section 4.3. Fig. 12 shows the range change due to this modeled complete poro-elastic relaxation. The resulting surface deformation field near the June 17 fault shows a heterogeneous pattern that is not present in the corresponding model of Jónsson et al. (2003, their Fig. 2b). Furthermore, the areas of large modeled range change due to poro-elastic relaxation (Fig. 12) are located near the fault segments with high surface slip estimated in our co-seismic inversion for the June 17 fault (Fig. 8a). Thus, our node-based parameterization of slip appears to be more consistent with the slip discontinuities near the surface. Explaining the heterogeneities in the post-seismic signal shown in Fig. 2d near the June 17 fault, and also in Fig. 2a of Jónsson et al. (2003), appears to require accounting for the structural details of the weak sedimentary layer and the segmentation in the surface fault trace. Such a study would also require a more thorough, time-dependent, description of the post-seismic deformation, as discussed below.

6.2. Interactions of post-seismic processes

Regarding poro-elastic relaxation after the June 17 earthquake, we have tried to reproduce the post-seismic signal near the June 17 fault (Fig. 2d) by allowing the change in Poisson's ratio to vary in space. Even by adding many free parameters, we cannot improve upon the

simple model of Jónsson et al. (2003) which explains only 50% of the variance in the observed signal (Dubois, 2006). In other words, the small, but significant, details of the signature cannot be explained by adding spatial complexity to a model without time dependence. A thorough, time-dependent, poro-elastic formulation is required.

Accordingly, a quasi-static approximation of poro-elastic deformation should not be used to "correct" GPS measurements of post-seismic displacements in the near field. Our numerical modeling suggests that the errors in the poro-elastic effect could be as large as 1 to 2 cm (Dubois, 2006). For example, the viscosity estimate for the 2000–2001 time interval (Árnadóttir et al., 2005) depends implicitly on the poro-elastic model. Although the "correction" applies to only a few GPS stations near the fault, the error could bias the estimate of viscosity by an order of magnitude in the worst case (Dubois, 2006).

Similarly, interactions between afterslip and viscous relaxation could also introduce errors if the two processes were analyzed separately. Indeed, the next step in future modeling should be a multi-process study (e.g., Freed et al., 2006).

6.3. Seismicity migration

In the SISZ, seismicity tends to migrate from east to west during an earthquake sequence, such that the distribution of aftershocks is asymmetric. Following the June 17 earthquake, more aftershocks occur on the west side of the fault than on the east side (Fig. 11). Furthermore, the aftershocks extend about 95 km to the west, but only about 15 km to the east of the June 17 mainshock epicenter. This phenomenon could be related to the geometric configuration, in particular the crustal thickening toward the east. Although the static co-seismic stress changes calculated in the "Iceland" configuration of the elastic model are slightly larger in the west than in the east, the asymmetry is too slight for this process to be the sole explanation (Fig. 11a). Similarly, the stress changes calculated by the completely relaxed poro-elastic approximation are not strong enough to produce the asymmetry observed in the seismicity (Fig. 11b). On the other hand, the distribution of stress changes due to viscous relaxation in the "Iceland" configuration of the visco-elastic model is asymmetric (Fig. 11c), but its shape differs from the east–west elongated pattern of seismicity in the SISZ in the 6 months following the June 2000 events. We should perhaps consider the aftershocks as active agents, rather than passive tracers, in the processes responsible for transferring stress from east to west across the SISZ. According to this notion, seismicity could have a kind of "domino effect", with a delay between events caused by rate- and state-dependent friction (e.g., Toda et al., 2005).

One process that does produce an asymmetric stress distribution is the geometric contribution due to the inter-seismic strain accumulation in the simple elastic model with a configuration that has a crust thickening to the east. Indeed, we imagine that the western part of the SISZ is closer to failure than the eastern part after about 100 years of inter-seismic deformation at a constant rate of strain (Fig. 11e). Combined with the effects of the co-seismic stress changes, this process could explain why a given mainshock tends to trigger more earthquakes to the west of its hypocenter than to the east (Fig. 11f).

6.4. June 21 triggering

Our calculations of the static Coulomb failure stress changes can elucidate the triggering of the June 21 event. All configurations of the elastic model show that the June 17 event increases Coulomb stress by 100 to 150 kPa at the subsequent location of the June 21 hypocenter. This result confirms that of a previous study (Árnadóttir et al., 2003) which assumed a homogeneous half-space configuration. In every case, stress increases over most of the modeled receiver fault that ruptured on June 21 (Fig. 13a). Although this effect can explain the location of the June 21 earthquake, it cannot explain the 3.5-day delay following the June 17 event.

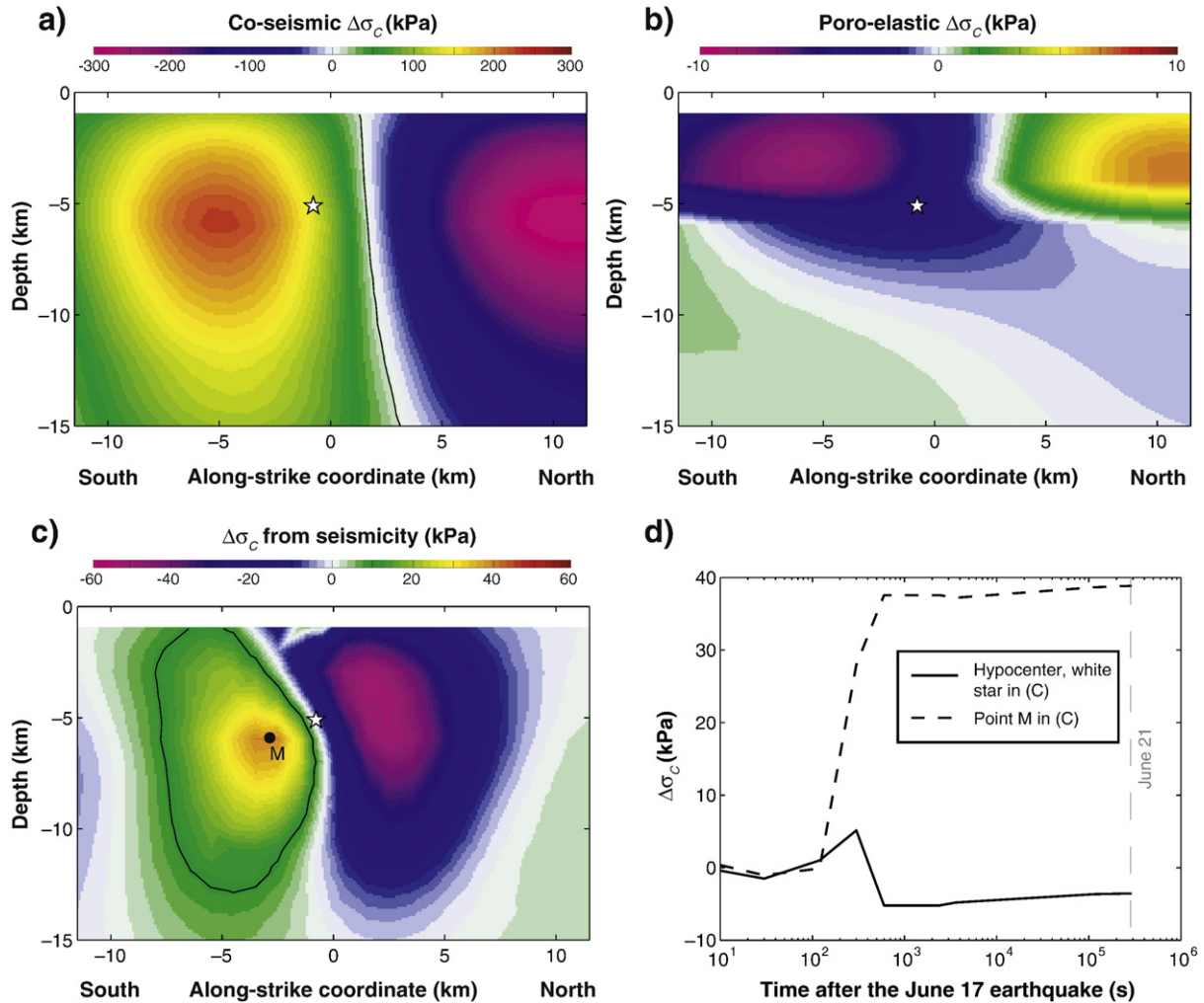


Fig. 13. Changes in Coulomb failure stress $\Delta\sigma_c$ on the modeled June 21 dislocation due to: (a) co-seismic June 17 deformation, (b) complete poro-elastic relaxation following the June 17 mainshock, and (c) summing the elastic co-seismic stresses for all the aftershocks with magnitude greater than zero between June 17 and June 21, but excluding the two $M_w=6$ mainshocks. The star indicates the position of the June 21 hypocenter and the black contour shows a 10 kPa increase of the Coulomb failure stress. (d) Time evolution of Coulomb failure stress due to the June 17 aftershocks at the location of the June 21 hypocenter (black) and at the location of maximum stress increase (dotted lines) corresponding to point M in (c).

Two other candidate processes, inter-seismic strain accumulation and viscous flow, are clearly too slow. Poro-elastic effects, on the other hand, can act on a time scale of the order of days for a fault zone with a thickness of the order of 10 to 100 m and a permeability of the order of 10^{-18} m^2 (Cocco and Rice, 2002). Using the quasi-static, completely relaxed approximation, we calculate the field of stress changes caused by poro-elastic relaxation following the June 17 earthquake (Fig. 13b). This process causes a stress decrease over large parts of the June 21 fault. Accordingly, we would not expect rupture to nucleate at the hypocenter of the June 21 earthquake. However, we have shown above that the assumptions underlying the quasi-static, completely relaxed approximation in terms of change in Poisson's ratio seem to be inappropriate here. We need a thorough, time-dependent, calculation to make strong conclusions about the poro-elastic process. Similarly, afterslip is a plausible candidate, but it also requires a time-dependent formulation to evaluate this post-seismic process (e.g., Perfettini et al., 1999).

The “domino” effect induced by cascading aftershocks may be an explanation. After the June 17 mainshock, the Coulomb failure stress also increases considerably on a large part of the June 21 modeled fault (Fig. 13c). Most of the increase comes from a magnitude 5 aftershock that occurred some 130 s after the June 17 mainshock at 15:42:50 UTC (Fig. 13d) midway between the two mainshock faults (Vogfjörð, 2003; Hjaltadóttir et al., 2005). Even if the mechanical process driving the

“domino” effect is not yet clear, this result highlights the importance of accounting for the large ($M>3$) aftershocks.

Finally, more than one process may be driving the triggering. For instance, one could imagine that the previous inter-seismic motion accumulated stress in the western part of the SISZ. Then some time-dependent afterslip and/or poro-elastic relaxation processes, which can have relaxation times of the order of a day, would induce cascading aftershocks in the preferred direction after the June 17 event. Ultimately, the combined effects of all these processes could have triggered the June 21 event. However, further numerical experiments in time-dependent three-dimensional modeling are required in order to test this hypothesis.

7. Conclusions and perspectives

We have analyzed the sensitivity of three quantities (co-seismic slip distribution, viscosity estimates, and stress change fields) to the structural heterogeneities which vary in space within the SISZ and evolve with time during the earthquake cycle for the sequence of earthquakes that occurred in June 2000. We have reached the following conclusions:

- 1) Structural heterogeneities play an important role. In inversions of measurements of co-seismic deformation, the slip distributions

are significantly deeper in realistic three-dimensional geometric configurations of the elastic model than in the conventional uniform half-space. The slip diminishes to negligible values of less than 50 cm below 12 km depth, supporting the notion that large earthquakes in the SISZ can rupture into the lower crust (Stefánsson et al., 1993). In the shallowest 2 km of the fault corresponding to a sedimentary layer, we find higher slip in the horizontally-layered configuration than in simpler configurations. This result highlights the need to account for a sedimentary layer and, as a next step, including the *en échelon* features of the fault trace geometry within it. A first attempt to include a weak fault damage zone leads to major changes in the resulting slip distribution, reducing the modeled seismic moment. Whereas the eastward thickening of the crust does not alter the previous results pertaining to the co-seismic analysis, it does modify the inter-seismic deformation and viscous relaxation. The results are important for assessing seismic hazard because realistic, heterogeneous configurations tend to show smaller stress changes in the uppermost part of the crust with asymmetrical distributions than do homogeneous, half-space configurations.

- 2) Aftershock seismicity plays an important role. Events with a magnitude $M > 3$ can have significant effects on Coulomb failure stress changes as well as on surface deformation. Accordingly, they should be considered in interpreting GPS and InSAR measurements, especially in post-seismic studies.
- 3) Realistic lithospheric models are required to explain the migration of seismicity across the SISZ. In particular, we suggest that accumulating inter-seismic strain in a simple elastic model with a configuration that includes an eastward-thickening crust can produce asymmetric perturbations in the stress field. The differences in the stress changes between a horizontal layering configuration and a variable crustal thickening configuration can raise the level of Coulomb failure stress to higher values in the western part than in the eastern part. This effect, combined with the co-seismic stress changes, might explain the tendency of seismicity to migrate from east to west across the SISZ during a single sequence of earthquakes. However, it would be necessary to improve this inter-seismic model in order to make stronger conclusions. Indeed, it is essential to include additional complexity, for example, a layered crust with variable thickness, a complete seismic cycle based on historical earthquake sequences, viscoplastic rheologies, or inter-seismic motion in the transform zones.
- 4) Static models cannot explain time-dependent behavior. For example, explaining the 4-day delay between the June 17 and June 21 mainshocks with a model with an ad hoc delay between aftershocks seems to be begging the question. Indeed, it is logically inconsistent to explain a time delay with a model that does not itself depend on time. In other words, the post-seismic processes operate on (at least) three different time scales: 4 days (between the June 17 to 21 earthquakes), 35 days (the 35-day and 70-day interferograms are quite similar), and ~1 year (aftershock decay). To be valid, a correct model will have to explain all these observations (e.g., Scholz, 2002; Brodsky and Prejean, 2005). We imagine a scenario that couples several processes. Prior to the June 17 mainshock, inter-seismic strain accumulation increases stress in the western part of the SISZ. Then some combination of time-dependent afterslip (Perfettini and Avouac, 2004), cascading aftershocks, and time-dependent poro-elastic relaxation (Masterlark, 2003), would further modify the stress field after the June 17 event. The effective time scale of these processes must be short, between $\sim 10^2$ s (to explain the magnitude 5 aftershocks) and $\sim 10^5$ s (to explain the 4-day delay until the June 21 event). Over time scales of months to years, the stress level must diminish to satisfy Omori's law of aftershock decay. Over still longer time scales of years to centuries, slower processes such as visco-elastic or plastic relaxation will come into play (Felzer and Brodsky, 2006).

To conclude, every study of the seismic cycle and seismic hazard estimation should include rheologic and geometric heterogeneities of the lithosphere in order to achieve accurate results. To improve the results, one should also consider multi-process models which explicitly allow stress and strain to vary with time (e.g., Freed et al., 2006).

Note added in proof:

On May 29, 2008, another earthquake occurred in the SISZ. According to the U.S. Geological Survey, the magnitude is $M_w = 6.2$ and the centroid is located at N64.037, W21.092, on the west edge of the SISZ.

Acknowledgments

We thank Charles Williams for generously providing the source code for his revised version of TECTON, as well as Frank Roth and his colleagues for the EDGRN/EDCMP and PSGRN/PSCMP codes. We also thank Eric Hetland, Tim Masterlark, Rikke Pedersen, Kristín Vogfjörð, Fred Pollitz, Sandra Richwalski, Páll Einarsson and Herb Wang for helpful discussions. Grimur Björnsson kindly explained the well data graciously provided by Iceland Geosurvey and Reykjavik Energy. Kristín Vogfjörð and Ragnar Stefánsson provided the relocated earthquake data set estimated by the Icelandic Meteorological Office as part of the PREPARED project. The authors would like to thank Andrea Antonioli and an anonymous reviewer for comments that improved the manuscript. This work was financed in part by EU projects RETINA, PREPARED and FORESIGHT as well as French national programs GDR STRAINSAR and ANR HYDRO-SEISMO.

References

- Allen, R.M., Nolet, G., Morgan, W.J., Vogfjörð, K., Nettles, M., Ekström, G., Bergsson, B.H., Ertendsson, P., Foulger, G.R., Jakobsdóttir, S., Julian, B.R., Pritchard, M., Ragnarsson, S., Stefánsson, R., 2002. Plume-driven plumbing and crustal formation in Iceland. *J. Geophys. Res.* 107 (B8), 2163–2181.
- Antonioli, A., Belardinelli, M.E., Bizzarri, A., Vogfjörð, K.S., 2006. Evidence of instantaneous dynamic triggering during the seismic sequence of year 2000 in south Iceland. *J. Geophys. Res.* 111 (B3), B03302.
- Árnadóttir, T., Olsen, K.B., 2000. Simulation of surface velocities and stress changes for the $M_s = 7.1$, 1784 earthquake, Iceland. Gudmundur Hafsteinnsson, Rit Vedurstofu Íslands, Reykjavík, Iceland.
- Árnadóttir, T., Hreinsdóttir, S., Gudmunsson, G., Einarsson, P., Heinert, M., Völksen, C., 2001. Crustal deformation measured by GPS in the South Iceland Seismic Zone due to two large earthquakes in June 2000. *Geophys. Res. Lett.* 28 (21), 4031–4033.
- Árnadóttir, T., Pedersen, R., Jónsson, S., Gudmundsson, G.B., 2003. Coulomb stress changes in the South Iceland Seismic Zone due to two large earthquakes in June 2000. *Geophys. Res. Lett.* 30 (5), 1205–1208.
- Árnadóttir, T., Geirsson, H., Einarsson, P., 2004. Coseismic stress changes and crustal deformation on the Reykjanes Peninsula due to triggered earthquakes on 17 June 2000. *J. Geophys. Res.* 109 (B9), B09307.
- Árnadóttir, T., Jónsson, S., Pollitz, F., Jiang, W., Feigl, K.L., 2005. Post-seismic deformation following the June 2000 earthquake sequence in the south Icelandic seismic zone. *J. Geophys. Res.* 110 (B12), B12308.
- Árnadóttir, T., Jiang, W., Feigl, K.L., Geirsson, H., Sturkell, E., 2006. Kinematic models of plate boundary deformation in southwest Iceland derived from GPS observations. *J. Geophys. Res.* 111 (B7), B07402.
- Barka, A., 1996. Slip distribution along the North Anatolian fault associated with large earthquakes of the period 1939–1967. *Bull. Seismol. Soc. Am.* 86 (5), 1238–1254.
- Bellou, M., Bergerat, F., Angelier, J., Homberg, C., 2005. Geometry and segmentation mechanisms of the surface traces associated with the 1912 Selsund Earthquake, Southern Iceland. *Tectonophysics* 404, 133–149.
- Bjarnason, I.T., Cowie, P., Anders, M.H., Seeber, L., Scholz, C.H., 1993a. The 1912 Iceland earthquake rupture: growth and development of a nascent transform system. *Bull. Seismol. Soc. Am.* 83 (2), 416–435.
- Bjarnason, I.T., Menke, W., Flóvenz, O., Caress, D., 1993b. Tomographic image of the mid-Atlantic plate boundary in southwestern Iceland. *J. Geophys. Res.* 98 (B4), 6607–6622.
- Björnsson, G., Flóvenz, Ó.G., Saemundsson, K., Einarsson, E.M., 2001. Pressure changes in Icelandic geothermal reservoirs associated with two large earthquakes in June 2000. Twenty-sixth Workshop on Geothermal Reservoir Engineering SGP-TR-168, Stanford University, USA, pp. 327–334.
- Bödvarsson, R., Rögnvaldsson, S.T., Slunga, R., Kjartansson, E., 1999. The SIL data acquisition system – at present and beyond year 2000. *Phys. Earth Planet. Inter.* 113, 89–101.

- Brodsky, E.E., Prejean, S.G., 2005. New constraints on mechanisms of remotely triggered seismicity at Long Valley Caldera. *J. Geophys. Res.* 110 (B4), B04302.
- Cattin, R., Briole, P., Lyon-Caen, H., Bernard, P., Pinettes, P., 1999. Effects of superficial layers on coseismic displacements for a dip-slip fault and geophysical implications. *Geophys. J. Int.* 137, 149–158.
- Cianetti, S., Giunchi, C., Cocco, M., 2005. Three-dimensional finite element modeling of stress interaction: an application to Landers and Hector Mine fault systems. *J. Geophys. Res.* 110 (B5), B05S17.
- CIG, Computational Infrastructure for Geodynamics, 2008 (<http://www.geodynamics.org>).
- Clifton, A., Einarsson, P., 2005. Styles of surface rupture accompanying the June 17 and 21, 2000 earthquakes in the South Iceland seismic zone. *Tectonophysics* 396 (3–4), 141–159.
- Clifton, A.E., Pagli, C., Jonsdottir, J.F., Eythorsdottir, K., Vogfjord, K., 2003. Surface effects of triggered fault slip on Reykjanes Peninsula, SW Iceland. *Tectonophysics* 369, 145–154.
- Cocco, M., Rice, J.R., 2002. Pore pressure and poroelasticity effects in Coulomb stress analysis of earthquake interactions. *J. Geophys. Res.* 107 (B2), 2630–2646.
- Cocco, M., Rice, J.R., 2003. Corrections to "Pore pressure and poroelasticity effects in Coulomb stress analysis of earthquake interactions". *J. Geophys. Res.* 108 (B2), 2069.
- Darbyshire, F.A., Bjarnason, I.T., White, R.S., Flóvenz, Ó.G., 1998. Crustal structure above the Iceland mantle plume imaged by the ICEMELT refraction profile. *Geophys. J. Int.* 135, 1131–1149.
- Darbyshire, F.A., White, R.S., Priestley, K.F., 2000. Structure of the crust and uppermost mantle of Iceland from combined seismic and gravity study. *Earth Planet. Sci. Lett.* 181, 409–428.
- DeMets, C., Gordon, R.G., Argus, D.F., Stein, S., 1990. Current plate motions. *Geophys. J. Int.* 101, 425–478.
- DeMets, C., Gordon, R.G., Argus, D.F., Stein, S., 1994. Effect of the recent revisions to the geomagnetic reversal time scale on estimates of current plate motions. *Geophys. Res. Lett.* 21, 2191–2194.
- Dhatt, G., Touzot, G., 1984. *The Finite Element Method Displayed*. John Wiley and Sons, New-York, USA, 526 pp.
- Du, Z., Foulger, G.R., 2001. Variation in the crustal structure across central Iceland. *Geophys. J. Int.* 145, 246–264.
- Dubois, L., 2006. Mechanical study of the June 2000 south Icelandic crisis based on 3D finite element models: rheological and geometrical effects. Ph.D. thesis, Université Paul Sabatier, Toulouse III, France, 230 pp. Available on <http://tel.archives-ouvertes.fr/tel-00268203/fr>.
- Efron, B., Tibshirani, R., 1986. Bootstrap methods for standard errors, confidence intervals, and other measures of statistical accuracy. *Stat. Sci.* 1 (1), 54–77.
- Einarsson, P., Sæmundsson, K., 1987. Earthquake epicenters 1982–1985 and volcanic systems in Iceland. In: Sigfusson, T.I. (Ed.), *Festschrift for Th. Sigurgeirsson*. Menningarsjodur, Reykjavik, Iceland.
- Einarsson, P., Björnsson, S., Foulger, G., Stefánsson, R., Skaftadóttir, T., 1981. Seismicity pattern in the south Iceland seismic zone. In: Simpson, D., Richards, P. (Eds.), *Earthquake Prediction – an International Review*. M. Ewing Ser. 4. American Geophysical Union, Washington, D.C., USA, pp. 141–151.
- Ekström, G., Dziewonski, A., Maternovskaya, N., Nettles, M., 2005. Centroid-moment tensor project. *Harvard Seismology*. <http://www.seismology.harvard.edu/projects/CMT>.
- Feigl, K.L., Dupré, E., 1999. RINGCHN: a program to calculate displacement components from dislocations in an elastic half-space with applications for modeling geodetic measurements of crustal deformation. *Comput. Geosci.* 25 (6), 695–704.
- Felzer, K.R., Brodsky, E.E., 2006. Decay of aftershocks density with distance indicates triggering by dynamic stress. *Nature* 441, 735–738.
- Fernández, J., Yu, T.T., Rundle, J.B., 1996. Horizontal viscoelastic-gravitational displacement due to a rectangular dipping thrust fault in a layered Earth model. *J. Geophys. Res.* 101 (B6), 13581–13594.
- Fialko, Y., 2004. Evidence of fluid-filled upper crust from observations of postseismic deformation due to the 1992 Mw = 7.3 Landers earthquake. *J. Geophys. Res.* 109 (B8), B08401.
- Flóvenz, Ó.G., Gunnarsson, K., 1991. Seismic crustal structure in Iceland and surrounding area. *Tectonophysics* 189, 1–17.
- Foulger, G.R., Du, Z., Julian, B.R., 2003. Iceland-type crust. *Geophys. J. Int.* 155 (2), 567–590.
- Freed, A.M., Bürgmann, R., Calais, E., Freymueller, J., Hreinsdóttir, S., 2006. Implications of deformation following the 2002 Denali, Alaska, earthquake for postseismic relaxation processes and lithospheric rheology. *J. Geophys. Res.* 111 (B1), B01401.
- Freymueller, J., King, N.E., Segall, P., 1994. The co-seismic slip distribution of the Landers earthquake. *Bull. Seismol. Soc. Am.* 84 (3), 646–659.
- Gebrande, H., Miller, H., Einarsson, P., 1980. Seismic structure of Iceland along RRISP profile 1. *J. Geophys. Res.* 85, 239–249.
- Hackman, M.C., King, G.C.P., Bilham, R., 1990. The mechanics of the south Iceland seismic zone. *J. Geophys. Res.* 95 (B11), 17339–17351.
- Hearn, E.H., Bürgmann, R., 2005. The effect of elastic layering on inversions of GPS data for coseismic slip and resulting stress changes: strike-slip earthquakes. *Bull. Seismol. Soc. Am.* 95 (5), 1637–1653.
- Helmstetter, A., Kagan, Y.Y., Jackson, D.D., 2005. Importance of small earthquakes for stress transfers and earthquake triggering. *J. Geophys. Res.* 110 (B5), B05S08.
- Hjaltadóttir, S., Vogfjörð, K.S., Slunga, R., 2005. Mapping subsurface faults in southwest Iceland using relatively located microearthquakes. Abstract EGU05-A-06664. European Geosciences Union – General Assembly, Vienna, Austria. *Geophysical Research Abstracts*, vol. 7.
- Hubert-Ferrari, A., Barka, A., Jacques, E., Nalbant, S.S., Meyer, B., Armijo, R., Tapponnier, P., King, G.C.P., 2000. Seismic hazard in the Marmara Sea region following the 17 August 1999 Izmit earthquake. *Nature* 404, 269–273.
- Hudnut, K.W., Shen, Z., Murray, M., McClusky, S., King, R., Herring, T., Hager, B., Feng, Y., Fang, P., Donnellan, A., 1996. Co-seismic displacements of the 1994 Northridge, California, earthquake. *Bull. Seismol. Soc. Am.* 86 (1B), S019–S036.
- IMO, Icelandic Meteorological Office, 2006 (<http://www.vedur.is/english/>).
- Jónsson, S., Segall, P., Pedersen, R., Björnsson, G., 2003. Post-earthquake ground movements correlated to pore-pressure transients. *Nature* 424, 179–183.
- Kaban, M.K., Flóvenz, Ó.G., Pálmason, G., 2002. Nature of the crust–mantle transition zone and the thermal state of the upper mantle beneath Iceland from gravity modelling. *Geophys. J. Int.* 149, 281–299.
- King, G.C.P., Stein, R.S., Lin, J., 1994. Static stress changes and the triggering of earthquakes. *Bull. Seismol. Soc. Am.* 84 (3), 935–953.
- Komatitsch, D., Liu, Q., Tromp, J., Süß, P., Stidham, C., Shaw, J.H., 2004. Simulations of ground motion in the Los Angeles Basin based upon the spectral-element method. *Bull. Seismol. Soc. Am.* 94 (1), 187–206.
- Lawson, C.L., Hanson, B.J., 1974. *Solving Least Squares Problems*. Prentice-Hall, Englewood Cliffs, USA, 337 pp.
- Masterlark, T., 2003. Finite element model predictions of static deformation from dislocation sources in a subduction zone: sensitivities to homogeneous, isotropic, Poisson-solid, and half-space assumptions. *J. Geophys. Res.* 108 (B11), 2540–2556.
- Masterlark, T., DeMets, C., Wang, H.F., Sánchez, O., Stock, J., 2001. Homogeneous vs. realistic heterogeneous subduction zone models: coseismic and postseismic deformation. *Geophys. Res. Lett.* 28 (21), 4047–4050.
- Melosh, H.J., Raefsky, A., 1981. A simple and efficient method for introducing faults into finite element computations. *Bull. Seismol. Soc. Am.* 71 (5), 1391–1400.
- Menke, W., 1999. Crustal isostasy indicates anomalous densities beneath Iceland. *Geophys. Res. Lett.* 26 (9), 1215–1218.
- Menke, W., Brandsdóttir, B., Einarsson, P., Bjarnason, I.T., 1996. Reinterpretation of the RRISP-77 Iceland shear wave profiles. *Geophys. J. Int.* 126, 166–172.
- Menke, W., West, M., Brandsdóttir, B., Sparks, D., 1998. Compressional and shear velocity structure of the lithosphere in the northern Iceland. *Bull. Seismol. Soc. Am.* 88, 1561–1571.
- Noir, J., Jacques, E., Békri, S., Adler, P.M., Tapponnier, P., King, G.C.P., 1997. Fluid flow triggered migration of events in the 1989 Dobi earthquake sequence of Central Afar. *Geophys. Res. Lett.* 24 (18), 2335–2338.
- Nur, A., Booker, J.R., 1972. Aftershocks caused by pore fluid flow? *Science* 175 (4024), 885–887.
- Okada, Y., 1985. Surface deformation to shear and tensile faults in a half-space. *Bull. Seismol. Soc. Am.* 75 (4), 1135–1154.
- Pagli, C., Pedersen, R., Sigmundsson, F., Feigl, K.L., 2003. Triggered fault slip on June 17, 2000 on the Reykjanes Peninsula, SW-Iceland captured by radar interferometry. *Geophys. Res. Lett.* 30 (6), 1273. doi:10.1029/2002GL015310.
- Pálmason, G., 1971. Crustal structure of Iceland from explosion seismology. *Soc. Sci. Iceland* XL 187.
- Parsons, T., Toda, S., Stein, R.S., Barka, A., Dieterich, J.H., 2000. Heightened odds of large earthquakes near Istanbul: an interaction-based probability calculation. *Science* 288 (5466), 661–665.
- Pedersen, R., Sigmundsson, F., Feigl, K.L., Árnadóttir, T., 2001. Coseismic interferograms of two MS = 6.6 earthquakes in the South Iceland Seismic Zone, June 2000. *Geophys. Res. Lett.* 28 (17), 3341–3344.
- Pedersen, R., Jónsson, S., Árnadóttir, T., Sigmundsson, F., Feigl, K.L., 2003. Fault slip distribution of two June 2000 Mw6.5 earthquakes in South Iceland estimated from joint inversion of InSAR and GPS measurements. *Earth Planet. Sci. Lett.* 213 (3–4), 487–502.
- Peltzer, G., Rosen, P., Rogez, F., Hudnut, K., 1998. Poroelastic rebound along the Landers 1992 earthquake surface rupture. *J. Geophys. Res.* 103 (B12), 30131–30146.
- Perfettini, H., Avouac, J.P., 2004. Postseismic relaxation driven by brittle creep: a possible mechanism to reconcile geodetic measurements and the decay rate of aftershocks, application to the Chi-Chi earthquake, Taiwan. *J. Geophys. Res.* 109 (B2), B02304.
- Perfettini, H., Stein, R.S., Simpson, R., Cocco, M., 1999. Stress transfer by the 1988–1989 M = 5.3 and 5.4 Lake Elsmar foreshocks to the Loma Prieta fault: unclamping at the site of peak mainshock slip. *J. Geophys. Res.* 104 (B9), 20169–20182.
- Pollitz, F.F., Sacks, I.S., 1996. Viscosity structure beneath northeast Iceland. *J. Geophys. Res.* 101 (B8), 17771–17793.
- Rice, J.R., Cleary, M.P., 1976. Some basic stress diffusion solutions for fluid saturated elastic porous media with compressible constituents. *Rev. Geophys.* 14 (2), 227–241.
- Rundle, J.B., 1982. Viscoelastic-gravitational deformation by a rectangular thrust fault in a layered Earth. *J. Geophys. Res.* 87 (9), 7787–7796.
- Scholz, C.H., 1990. *The Mechanics of Earthquakes and Faulting*. Cambridge University Press, Cambridge, UK, 439 pp.
- Scholz, C.H., 2002. *The Mechanics of Earthquakes and Faulting*. Cambridge University Press, Cambridge, UK, 471 pp.
- Sigmundsson, F., 1991. Post-glacial rebound and asthenosphere viscosity in Iceland. *Geophys. Res. Lett.* 18 (6), 1131–1134.
- Sigmundsson, F., Einarsson, P., 1992. Glacio-isostatic crustal movements caused by historical volume change of the Vatnajökull ice cap, Iceland. *J. Geodyn.* 19 (21), 2123–2126.
- Sigmundsson, F., Einarsson, P., Bilham, R., Sturkell, E., 1995. Rift-transform kinematics in south Iceland: deformation from Global Positioning System measurements, 1986 to 1992. *J. Geophys. Res.* 100 (B4), 6235–6248.
- Slunga, R., 2003. Microearthquakes analysis at local seismic networks in Iceland and Sweden and earthquake precursors. In: Takanami, T., Kitagawa, G. (Eds.), *Methods and Applications of Signal Processing in Seismic Network Operations*. Springer-Verlag, Germany, pp. 149–173.

- Slunga, R., Rögnvaldsson, S.T., Böldvarsson, R., 1995. Absolute and relative locations of similar events with application to microearthquakes in southern Iceland. *Geophys. J. Int.* 123, 409–419.
- Staples, R.K., White, R.S., Brandsdóttir, B., Menke, W., Maguire, P.K.H., McBride, J.H., 1997. Färoe-Iceland Ridge Experiment 1. Crustal structure of northeastern Iceland. *J. Geophys. Res.* 102 (B4), 7849–7866.
- Stefánsson, R., 2006. PREPARED Final Report. European Report, Icelandic Meteorological Office, Reykjavík, Iceland. Available on <http://www.vedur.is/utgafa/greinargerdir/2006/06009.pdf>.
- Stefánsson, R., Böldvarsson, R., Slunga, R., Einarsson, P., Jakobsdóttir, S., Bungum, H., Gregersen, S., Havskov, J., Hjelme, J., Korhonen, H., 1993. Earthquake prediction research in the South Iceland seismic zone and the SIL Project. *Bull. Seismol. Soc. Am.* 83 (3), 696–716.
- Stein, R.S., 1999. The role of stress transfer in earthquake occurrence. *Nature* 402 (6762), 605–609.
- Stein, R.S., Barka, A.A., Dieterich, J.H., 1997. Progressive failure on the North Anatolian fault since 1939 by earthquake stress triggering. *Geophys. J. Int.* 128, 594–604.
- Tarantola, A., 2005. *Inverse Problem Theory and Methods for Model Parameter Estimation*. SIAM, Philadelphia, USA, 342 pp.
- Thoma, M., Wolf, D., 2001. Inverting land uplift near Vatnajökull, Iceland, in terms of lithosphere thickness and viscosity stratification. In: Sideris, M.G. (Ed.), *Gravity, Geoid and Geodynamics 2000*. Springer-Verlag, Berlin, Germany, pp. 97–102.
- Toda, S., Stein, R.S., Richards-Dinger, K., Bozkurt, S.B., 2005. Forecasting the evolution of seismicity in southern California: animations built on earthquake stress transfer. *J. Geophys. Res.* 110 (B5), B05S16.
- Tryggvason, A., Rögnvaldsson, S.T., Flóvenz, Ó.G., 2002. Three-dimensional imaging of the P- and S- wave velocity structure and earthquake locations beneath Southwest Iceland. *Geophys. J. Int.* 151, 848–866.
- Vogfjörð, K., 2003. Triggered seismicity after the June 17, Mw = 6.5 earthquake in the South Iceland Seismic Zone: the first five minutes. Abstract 11251. EGS - AGU - EUG Joint Assembly, Nice, France. *Geophysical Research Abstracts*, vol. 5.
- Wang, H.F., 2000. *Theory of Poroelasticity with Applications to Geomechanics and Hydrology*. Princeton Univ. Press, Princeton, USA, 287 pp.
- Wang, R., Lorenzo-Martín, F., Roth, F., 2003. Computation of deformation induced by earthquakes in a multi-layered crust — FORTRAN programs EDGRN/EDCMP. *Comput. Geosci.* 29 (2), 195–207.
- Wang, R., Lorenzo-Martín, F., Roth, F., 2006. PSGRN/PSCMP — a new code for calculating co-postseismic deformations and geopotential changes based on the viscoelastic-gravitational dislocation theory. *Comput. Geosci.* 32 (4), 527–541.
- Weir, N.R.W., White, R.S., Brandsdóttir, B., Einarsson, P., Shimamura, H., Shiobara, H., RISE Fieldwork Team, 2001. Crustal structure of the northern Reykjanes Ridge and the Reykjanes Peninsula, southwest Iceland. *J. Geophys. Res.* 106 (B4), 6347–6368.
- Wells, D.L., Coppersmith, K.J., 1994. New empirical relationships among magnitude, rupture length, rupture width, rupture area, and surface displacement. *Bull. Seismol. Soc. Am.* 84, 974–1002.
- Welstead, S.T., 1999. *Fractal and Wavelet Image Compression Techniques*. SPIE Optical Engineering Press, Bellingham, Washington, USA, 232 pp.
- Williams, C.A., Richardson, R.M., 1991. A rheologically layered three-dimensional model of the San Andreas fault in central and southern California. *J. Geophys. Res.* 96 (B10), 16597–16623.